

AD-A143 440

BOUNDARY-LAYER DEVELOPMENT ON SHIP HULLS(U) DCW
INDUSTRIES SHERMAN OAKS CA D C WILCCX JAN 83
DCW-R-26-01 N00014-81-C-0235

1/1

UNCLASSIFIED

F/G 20/4

NL

DTW INDUSTRIAL

END

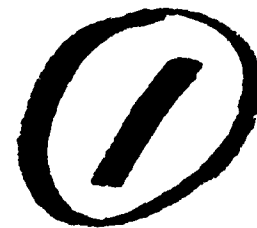
FILMED

DTIC



•

AD-A143 440



BOUNDARY-LAYER DEVELOPMENT

ON CHIP HULL

David C. Wilson

DCW INDUSTRIES

DTIC
ELECTE

JUL 25 1984

S

D

FILE COPY

4367 TROOST AVENUE, STUDIO CITY, CALIFORNIA 91604

DISTRIBUTION STATEMENT A

Approved for public release;
Distribution Unlimited

84 07 24 077

BOUNDARY-LAYER DEVELOPMENT
ON SHIP HULLS

by

David C. Wilcox

FINAL SCIENTIFIC REPORT
January 1983

Prepared Under Contract N00014-81-C-0235

for the

GENERAL HYDRODYNAMICS RESEARCH PROGRAM

OF THE NAVAL SHIP SYSTEMS COMMAND

NAVAL SHIP RESEARCH AND DEVELOPMENT CENTER

Accession For	
NTIS GRA&I	<input checked="" type="checkbox"/>
DTIC TAB	<input type="checkbox"/>
Unannounced	<input type="checkbox"/>
Distribution/	
City Codes	
and/or	
Dist.	
A/1	

DCW Industries, Inc.

4367 Troost Avenue
Studio City, California 91604
213/769-7571 or 213/790-3844

DISTRIBUTION STATEMENT A

Approved for public release;
Distribution unlimited

DTIC
SELECTED
JUL 25 1984

D

UNCLASSIFIED

SECURITY CLASSIFICATION OF THIS PAGE (When Data Entered)

REPORT DOCUMENTATION PAGE		READ INSTRUCTIONS BEFORE COMPLETING FORM
1. REPORT NUMBER	2. GOVT ACCESSION NO.	3. REPORTS CATALOG NUMBER
4. TITLE (and Subtitle) BOUNDARY-LAYER DEVELOPMENT ON SHIP HULLS		5. TYPE OF REPORT & PERIOD COVERED FINAL REPORT 1 FEB 1981 - 31 JAN 1983
		6. PERFORMING ORG REPORT NUMBER DCW-R-26-01
7. AUTHOR(s) DAVID C. WILCOX		8. CONTRACT OR GRANT NUMBER N00014-81-C-0035
9. PERFORMING ORGANIZATION NAME AND ADDRESS DCW INDUSTRIES, INC. 4367 Troost Avenue Studio City, CA 91604		10. PROGRAM ELEMENT PROJECT TASK AREA & WORK UNIT NUMBERS
11. CONTROLLING OFFICE NAME AND ADDRESS DTNSRDC Bethesda, MD		12. REPORT DATE JANUARY 1983
		13. NUMBER OF PAGES 121
14. MONITORING AGENCY NAME & ADDRESS (if different from Controlling Office)		15. SECURITY CLASS (of this report) UNCLASSIFIED
		15a. DECLASSIFICATION DOWNGRADING SCHEDULE
16. DISTRIBUTION STATEMENT (of this Report) Approved for Public Release, Distribution Unlimited.		
17. DISTRIBUTION STATEMENT (of the abstract entered in Block 20, if different from Report)		
18. SUPPLEMENTARY NOTES		
19. KEY WORDS (Continue on reverse side if necessary and identify by block number) SHIP HYDRODYNAMICS, THREE-DIMENSIONAL BOUNDARY LAYERS, THICK BOUNDARY LAYERS		
20. ABSTRACT (Continue on reverse side if necessary and identify by block number) A three-dimensional boundary-layer computer program is developed which is suitable for application to arbitrary ship hulls. The program embodies the Wilcox-Rubesin two-equation model of turbulence. The numerical algorithm, based on the Elottner variable-grid method and the Krause explicit marching technique, is tested for two ship hulls and found to be accurate and stable for relatively large reverse crossflow. The program admits		

DD FORM 1 JAN 73 1473

EDITION OF 1 NOV 65 IS OBSOLETE

UNCLASSIFIED

SECURITY CLASSIFICATION OF THIS PAGE (When Data Entered)

rapid stretching of the grid normal to the surface and solutions become grid independent for mesh-point number in excess of about 60.

Comparisons between computed and measured momentum thickness for the two ship-hull computations indicate that, on the one hand, the Wilcox-Rubesin model improves predictive accuracy over that found at the 1980 SSPA-ITTC Workshop on Ship Boundary Layers. On the other hand, discrepancies between computation and measurement remains large enough to warrant further research. Because the computations use conventional thin-shear-layer approximations and discrepancies are largest near the stern, it appears likely that improved accuracy can only be obtained by accounting for the fact that the boundary layer becomes "thick".

To test the model for thick boundary layers, three submerged axisymmetric bodies are analyzed, viz, a thin cylinder aligned axially with the freestream and two bodies with adverse pressure gradient. Comparisons between computed and measured flow properties for the thin cylinder show the model to be quite accurate in the absence of pressure gradient. Using first the measured surface pressure distribution and then the measured boundary-layer-edge pressure distribution, experimental data are found to lie between the two computational results for both bodies. This result indicates that by accounting for the normal pressure gradient, model predictions for thick boundary layers should be very close to measurements. An integral method is devised and tested for computing the normal pressure gradient. Differences between computed and measured pressure distributions are well within experimental data scatter.

CONTENTS

SECTION	PAGE
ABSTRACT.....	11
CONTENTS.....	iv
1 INTRODUCTION.....	1
2 EQUATIONS OF MOTION.....	3
2.1 The Turbulence Model.....	3
2.2 Boundary Conditions.....	4
3 NUMERICAL CONSIDERATIONS.....	6
3.1 The Numerical Procedure.....	6
3.2 Preliminary Test of the Revised Program.....	9
3.3 Numerical Accuracy Study.....	14
4 SHIP-HULL APPLICATIONS.....	19
4.1 SSPA Model 720.....	19
4.1.1 Effect of Girthwise Integration Direction..	19
4.1.2 Effect of Mesh Refinement.....	20
4.1.3 Comparison of Computed and Measured Momentum Thickness.....	21
4.2 HSVA Tanker.....	23
5 ANALYSIS OF THE THICK BOUNDARY LAYER.....	26
5.1 Perturbation Analysis.....	26
5.1.1 Sublayer Scaling.....	26
5.1.2 Wall-Layer Scaling.....	28
5.2 Flow Past a Wire.....	30
5.3 Bodies with Adverse Pressure Gradient.....	35
5.3.1 Integral Properties.....	35
5.3.2 Velocity and Reynolds-Stress Profiles.....	38
5.3.3 Turbulence Properties.....	40
5.3.4 Streamline-Curvature Effects.....	40
5.4 Pressure Variation in a Thick Boundary Layer.....	44
6 DISCUSSION.....	50
REFERENCES.....	52
APPENDIX: PROGRAM LISTINGS.....	54
A.1 PROGRAM SHPMISH.....	54
A.2 PROGRAM VELOC.....	71
A.3 PROGRAM EDDY3.....	84

1. INTRODUCTION

Increasingly there is a need to more accurately predict the viscous resistance on ship hulls, particularly in light of modern-day fuel costs. The rapid increase in fuel costs cries out as a mandate to ship-hull designers to reduce hull resistance, both wave-making and viscous. Experience has shown that significant advances in design efficiency often require more sophisticated design tools, and in today's environment, particularly those of the computational variety.

Airplane and missile designers have had a great deal of success in developing and utilizing the concept of the "numerical wind tunnel". As both computational algorithms and accurate engineering sets of equations describing turbulent fluctuations and stresses have been developed and improved, so has the ability to replace expensive wind-tunnel tests by a series of computer runs. In addition to being relatively inexpensive, such numerical simulations can more exactly simulate full-scale flow conditions than can wind-tunnel tests.

In the ship context there is just as pressing a need to replace expensive tests by numerical simulations. In fact, in light of the inherent contradiction involved in trying to simultaneously match Froude and Reynolds numbers, then is an even more pressing need to utilize the "numerical towing tank" in the design process.

The state of the art of numerical simulations, including viscous effects, is further advanced in the aerodynamic context than it is in the hydrodynamic case. Conceptually this is sensible as the flow past a ship hull involves a free surface and is inherently three dimensional while, by contrast, much of the flow area over an airplane wing involves a homogeneous fluid and can be treated as two dimensional. This two dimensionality has been of especial value to aerodynamicists as they have been able to justify focusing on two-dimensional flows. A great deal of progress in improving computational efficiency has been made because of the relative

simplicity of a two-dimensional computation, progress which would have been much harder to achieve if the aerodynamicist's primary application had demanded focusing on three dimensionality. As a result, computing separated flows can be done today¹ at less than a percent of the cost seven or eight years ago². And, of course, these methods are now being implemented in three dimensions.

Even in three dimensions the aerodynamicist has an easier time of it than the hydrodynamicist because he needn't deal with a free surface. Nevertheless, the day of the numerical towing tank draws nearer and nearer. The purpose of this project has been to help in hastening the arrival of the numerical towing tank.

To accomplish this end, we have addressed the viscous portion of the problem. We have applied a widely-tested two-equation model of turbulence (Section 2) to (a) real ship hulls and (b) "thick" turbulent boundary layers on submerged axisymmetric bodies. The object of the ship-hull computations has been to test the model's accuracy in the limit of classical "thin-shear-layer" approximations. The latter computations have been done as an attempt to pinpoint the special characteristics of and to test the model for "thick" boundary layers.

In performing the analysis we have developed a new three-dimensional boundary-layer program appropriate to arbitrary ship hulls. A great deal of the effort in this project focused on devising an accurate numerical procedure compatible with the turbulence model equations. Section 3 presents details of the algorithm including a detailed accuracy study.

In Section 4 we present results of the two ship-hull computations, including comparison of computed and measured flow properties. Section 5 includes details of our thick-boundary-layer study. Results and conclusions follow in Section 6. The Appendix includes computer-program listings and an explanation of program input and output.

2. EQUATIONS OF MOTION

In this section we describe the Wilcox-Rubesin³ two-equation model of turbulence. First we summarize the equations of motion including all closure coefficients. Then, we state the boundary conditions appropriate to smooth and rough surfaces.

2.1 THE TURBULENCE MODEL

For an incompressible fluid of density, ρ , and kinematic viscosity, ν , we must solve the equations of mass and momentum conservation, viz,

$$\frac{\partial u_i}{\partial x_i} = 0 \quad (1)$$

$$u_j \frac{\partial u_i}{\partial x_j} = -\frac{1}{\rho} \frac{\partial p}{\partial x_i} + \frac{\partial}{\partial x_j} \left[\nu \frac{\partial u_i}{\partial x_j} + \tau_{ij} \right] \quad (2)$$

where steady flow conditions have been assumed. In Equations (1-2), u_i and x_i denote velocity and position vector, p is static pressure and τ_{ij} is the Reynolds-stress tensor. To close the system, τ_{ij} is assumed proportional to the mean strain rate tensor, S_{ij} , wherefore

$$\tau_{ij} = 2\epsilon S_{ij} - \frac{2}{3}k\delta_{ij} \quad (3)$$

where

$$S_{ij} \equiv \frac{1}{2} \left(\frac{\partial u_i}{\partial x_j} + \frac{\partial u_j}{\partial x_i} \right) \quad (4)$$

The quantity k is turbulent mixing energy and ϵ is kinematic eddy viscosity. The latter is defined in terms of k and the turbulent dissipation rate, ω , by

$$\epsilon = \gamma^* k / \omega \quad (5)$$

where γ^* is a closure coefficient. Finally, the turbulence parameters k and ω satisfy the following equations.

$$u_j \frac{\partial k}{\partial x_j} = \tau_{ij} \frac{\partial u_i}{\partial x_j} - \beta^* \omega k + \frac{\partial}{\partial x_j} \left[(\nu + \sigma^* \epsilon) \frac{\partial k}{\partial x_j} \right] \quad (6)$$

$$u_j \frac{\partial \omega^2}{\partial x_j} = \gamma \frac{\omega^2}{k} \tau_{1j} \frac{\partial u_1}{\partial x_j} - \left[\beta + 2\sigma \left(\frac{\partial \ell}{\partial x_k} \right)^2 \right] \omega^3 + \frac{\partial}{\partial x_j} \left[(v + \sigma \epsilon) \frac{\partial \omega^2}{\partial x_j} \right] \quad (7)$$

where ℓ is the turbulent length scale defined by:

$$\ell = k^{1/2} / \omega \quad (8)$$

Equations (5-7) contain six closure coefficients, viz, β , β^* , γ , γ^* , σ and σ^* . The values of these coefficients have been determined from very general arguments based on widely observed properties of turbulent flows. The values used in the present study are:

$$\left. \begin{aligned} \beta &= 3/20 & ; & & \beta^* &= 9/100 \\ \sigma &= 1/2 & ; & & \sigma^* &= 1/2 \\ \gamma^* &= 1 - (1 - \lambda^2) \exp(-Re_T) \\ \gamma \gamma^* &= \frac{10}{9} [1 - (1 - \lambda^2) \exp(-Re_T/4)] \\ \text{where } \lambda &= \frac{1}{11} \end{aligned} \right\} \quad (9)$$

In Equations (9), the quantity Re_T is the Reynolds number of the turbulence defined by

$$Re_T = \frac{k^{1/2} \ell}{\nu} = \frac{k}{\omega \nu} \quad (10)$$

2.2 BOUNDARY CONDITIONS

Application of the no-slip boundary condition yields

$$\left. \begin{aligned} u_1 &= 0 \\ k &= 0 \end{aligned} \right\} \text{ at solid boundaries} \quad (11)$$

The boundary conditions for ω appropriate to smooth and rough surfaces have been shown by Wilcox and Traci⁴ to be

$$\left. \begin{aligned} \omega &\rightarrow \frac{20\nu}{\beta y^2} \quad \text{as } y \rightarrow 0 & ; & \text{Smooth Surface} \\ \omega &= \frac{S}{\sqrt{\beta^*}} \frac{u_\tau^2}{\nu} \quad \text{at } y = 0 & ; & \text{Rough Surface} \end{aligned} \right\} \quad (12)$$

where u_τ is friction velocity and S is a function of dimensionless

roughness height $k^+ \equiv u_\tau k / \nu$ defined by

$$S = (36/k^+)^2 + (8/k^+)^{1/2} \quad (13)$$

Equations (1-13) completely define the turbulence model and surface boundary conditions. All analysis in this project has been done using Equations (1-13).

3. NUMERICAL CONSIDERATIONS

Because our primary interest in this project is in three-dimensional boundary layers, a substantial effort has gone into devising an accurate, stable and efficient numerical procedure for solving Equations (1-13) in the 3-D boundary layer. Few computer programs have been developed with sufficient generality for arbitrary ship-hull applications and we have, in effect, developed such a program from scratch.

Our original starting point was a generalized version of the 3-D boundary-layer program developed by Cebeci, et al⁵. The numerical procedure embodied in the program is based on Keller's⁶ "Box Method". After a great deal of numerical experimentation and frustration, we have concluded that the Box Method is incompatible with turbulence-model equations.

This is not to say the Box Method is deficient as a numerical scheme. On the contrary, the method has proven to be very efficient and very accurate in many applications. However, advanced turbulence models such as the one being used often require special numerical treatment. Over the years, we have found that many excellent, proven, numerical schemes just don't work well in solving the equations attending such a model. We now know the Box Method falls into this category.

To remedy this problem, we have completely rewritten the program. It now embodies a numerical method which has proven compatible with the turbulence model. In the following sections we first discuss the new numerical method. Next, we show typical numerical results for a flat-plate boundary layer, including comparisons with experimental data. Finally, we present results of a numerical accuracy study.

3.1 THE NUMERICAL PROCEDURE

For many years we have obtained accurate two-dimensional boundary layer solutions for our model equations using the classical Blotner⁷ method. Hence, we decided to extend the method to three

dimensions in hopes it would retain its desirable stability and accuracy characteristics. Before embarking on such a major re-programming effort we made a brief review of Blottner's more recent work. We found that, as an improvement to his original procedure, Blottner⁸ has devised his "Variable Grid" algorithm. This revised method offers far greater accuracy than his original method, particularly for very coarse finite-difference grids. We decided to use the improved algorithm.

In essence, the "Variable Grid" method uses a conservation form treatment for diffusion terms. That is, in the original Blottner method, diffusion terms must first be expanded according to:

$$\frac{\partial}{\partial y}(\epsilon \frac{\partial u}{\partial y}) = \epsilon \frac{\partial^2 u}{\partial y^2} + \frac{\partial \epsilon}{\partial y} \frac{\partial u}{\partial y} \quad (14)$$

Then, central difference approximations are used for $\partial u / \partial y$, $\partial \epsilon / \partial y$, and $\partial^2 u / \partial y^2$. By contrast, in the improved Blottner method, we write directly (subscripts denote mesh point number):

$$\left[\frac{\partial}{\partial y}(\epsilon \frac{\partial u}{\partial y}) \right]_j = \frac{\epsilon_{j+\frac{1}{2}} \delta u_{j+\frac{1}{2}} - \epsilon_{j-\frac{1}{2}} \delta u_{j-\frac{1}{2}}}{\frac{1}{2}(\Delta y_j + \Delta y_{j-1})} \quad (15)$$

$$\delta u_{j+\frac{1}{2}} = (u_{j+1} - u_j) / \Delta y_j \quad (16)$$

and similarly for $(\delta u)_{j-\frac{1}{2}}$. The quantity $\Delta y_j = y_{j+1} - y_j$ is the incremental change in the normal coordinate y . As will be shown in Subsection 3.3, this straightforward modification permits much greater stretching of the grid normal to the surface than is possible with the original Blottner method.

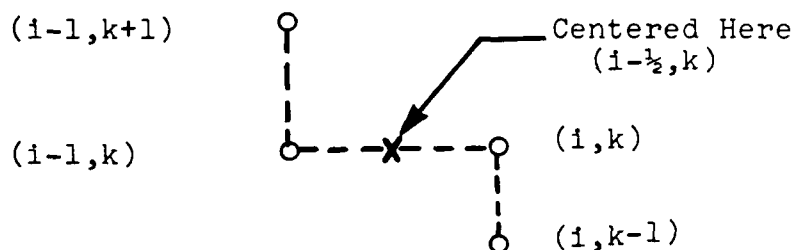
Thus far, we have spoken only of the direction normal to the surface. Because the three-dimensional boundary-layer equations have a real characteristic which is not necessarily aligned with the freestream flow direction, any accurate numerical procedure must be consistent with the attending zone of dependence. The original Box Method does not treat this problem properly and to avoid

future difficulties we decided to accomodate the zone-of-dependence feature in the revised numerical scheme. In an unpublished study, Wilcox and James⁹ devised a family of explicit, unconditionally stable marching methods which potentially could deal with this problem. A review of that study showed that most of the family were of first-order accuracy. However, one of the most promising of the family is second-order accurate. Another brief review of boundary-layer literature showed that this scheme has been used by many others in three-dimensional boundary-layer applications. The scheme is attributed to Krause¹⁰. We have opted to use Krause scheme in the revised program.

The essence of the Krause procedure is the manner in which cross-flow convective terms are treated. As an illustration, the term $w\partial u/\partial z$ (where u and w denote streamwise and crossflow velocity components and z is the crossflow coordinate) is discretized according to:

$$(w\partial u/\partial z)_{i-\frac{1}{2},k} = \frac{1}{2} w_{i-\frac{1}{2},k} \left(\frac{u_{i-1,k+1} - u_{i-1,k}}{\Delta z_k} + \frac{u_{i,k} - u_{i,k-1}}{\Delta z_{k-1}} \right) \quad (17)$$

where i and k denote mesh point number in the x and z directions, respectively, $\Delta z_k = z_{k+1} - z_k$, and the finite-difference molecule is as shown below.



This scheme is unconditionally stable for positive crossflow ($w > 0$) and conditionally stable for negative crossflow ($w < 0$), the stability condition being:

$$\frac{w\Delta x}{u\Delta z} > -1 \quad (18)$$

Thus, for equally spaced mesh points ($\Delta x = \Delta z$), this scheme is stable for negative crossflow angles up to 45 degrees from the streamwise direction.

3.2 PRELIMINARY TEST OF THE REVISED PROGRAM

A key difficulty encountered with the Box Method was the presence of large round-off errors in the equation for ω^2 . Even when we devised a special procedure to eliminate these errors (caused by the numerical method's inability to accurately compute the rapid variation in ω^2 as $y \rightarrow 0$), nontrivial oscillations in properties such as skin friction remained. All of these difficulties were encountered for the simplest boundary-layer of all, the two-dimensional flat-plate (constant pressure) boundary layer. Hence, as a preliminary test of our revised 3-D boundary-layer program, which we will refer to as EDDY3, we focus on the flat-plate boundary layer. We have done two computations, the first for a turbulent case and the second for a transitional case.

The first computation was initiated from approximate profiles at a plate-length Reynolds number, Re_x , of one million. Using 40 equally spaced streamwise steps, the computation proceeds to a plate-length Reynolds number of five million. This means the ratio of streamwise stepsize to boundary-layer thickness ranges from 1.3 to 6.8. Such large steps are comparable to those used in mixing-length computations. Only 61 mesh points were used normal to the surface with the grid-point incremental spacing increasing in a geometric progression with a progression ratio of $r = 1.11$.

Figure 1 compares computed skin friction, c_f , and momentum thickness Reynolds number, Re_θ , with the Karman-Schoenherr correlation. As shown, both c_f and Re_θ virtually duplicate the correlation. Figures 2 through 4 compare computed velocity, turbulent dissipation rate and turbulent mixing energy profiles with corresponding exact theoretical asymptotic sublayer and wall-layer (log region) profiles. In all cases, the numerical predictions clearly fall

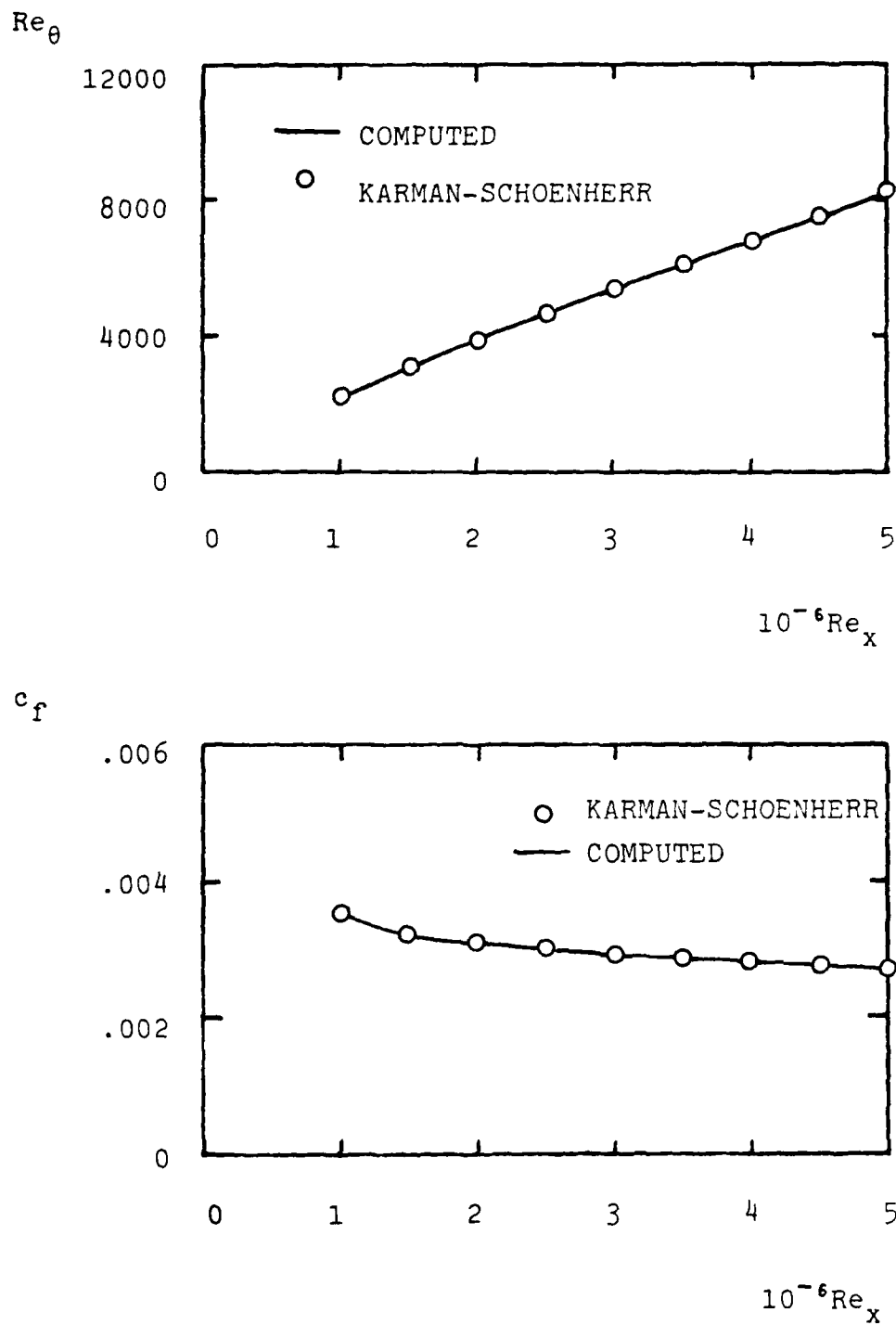


Figure 1. Comparison of computed and measured skin friction and momentum thickness for a flat-plate boundary layer; 61 mesh points and $r = 1.11$.

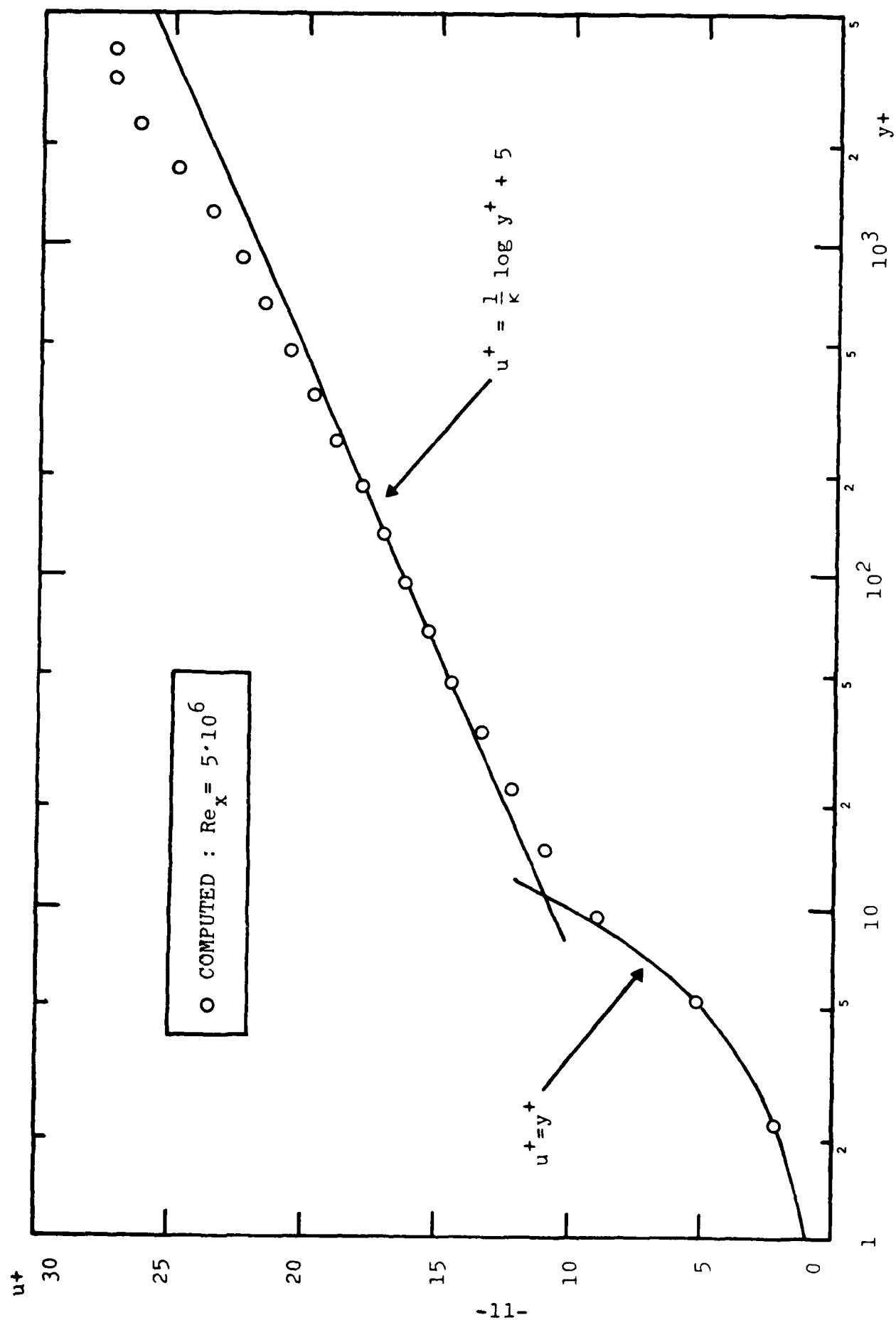


Figure 2. Comparison of computed velocity profile for a flat-plate boundary layer with theoretical asymptotic sublayer and wall-layer profiles; 61 mesh points and $r = 1.11$.

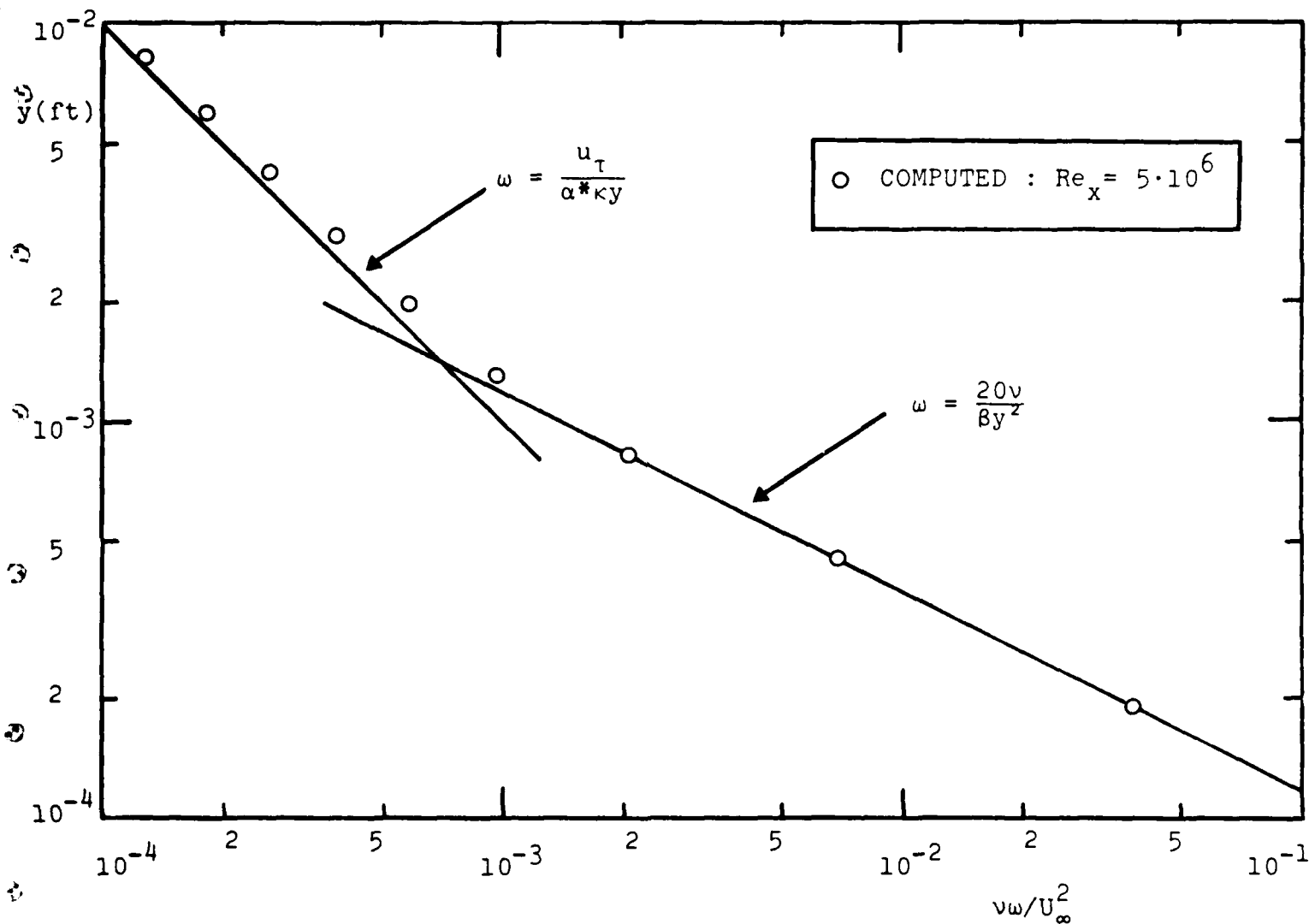


Figure 3. Comparison of computed specific dissipation rate profile for a flat-plate boundary layer with theoretical asymptotic sublayer and wall-layer profiles; 61 mesh points and $r = 1.11$.

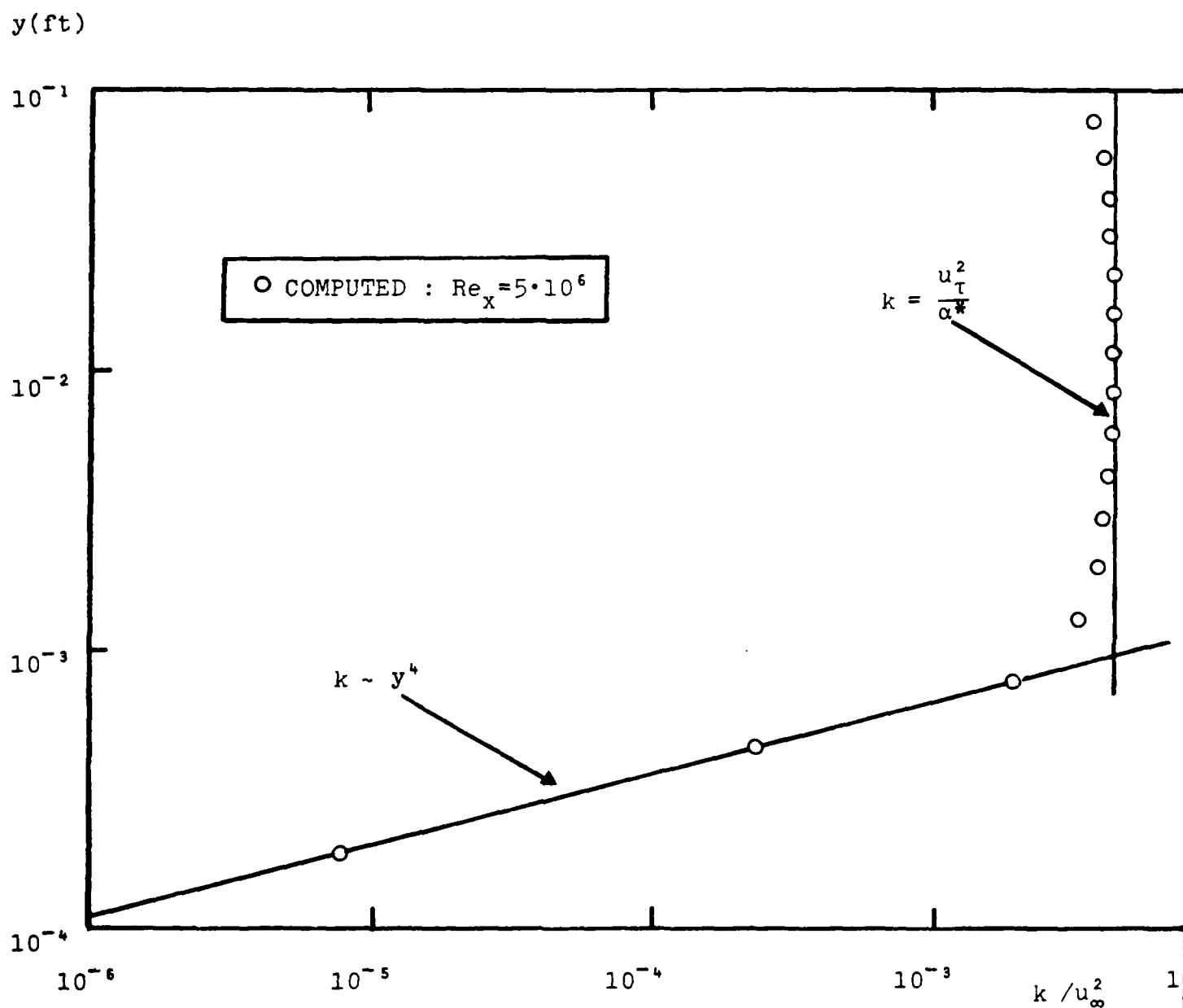


Figure 4. Comparison of computed turbulent mixing energy profile for a flat-plate boundary layer with theoretical asymptotic sublayer and wall-layer profiles; 61 mesh points and $r=1.11$.

very close to the asymptotic profiles, thus verifying the accuracy of the revised numerical procedure in the absence of crossflow.

For our second test we begin with laminar flow and integrate all the way through transition to test whether c_f oscillations attend such a computation. As shown in Figure 5, the revised program displays no such oscillations. Again, the geometric progression ratio used was $r = 1.11$.

In conclusion, the success achieved in these two flat-plate cases leaves us confident that we have a numerical procedure which is at once stable and accurate. While these computations fail to test the program's ability to handle reverse crossflow, the ship-hull applications of Section 4 indicate no difficulties are encountered, even with very large crossflow velocities.

2.3 NUMERICAL ACCURACY STUDY

Before proceeding to more complex applications, it is instructive to examine the sensitivity of EDDY3 computations to grid-point spacing. One of the most remarkable features of the revised program is that in past two-dimensional computations, at least 200 mesh points would have been needed to achieve mesh-independent solutions for an Re_x of five million. This is true because the original Blottner method is of questionable accuracy for values of r in excess of 1.04. To test the program's accuracy, we performed a series of turbulent flat-plate boundary-layer computations in which r was increased all the way to 1.40. To establish a baseline solution, we used our two-dimensional program to compute the flow of Subsection 3.2 with 200 mesh points and with $r = 1.03$.

Figure 6 shows the percent error in skin friction as a function of the progression ratio r . Remarkably, even with an r as large as 1.40 the c_f error is only 8.5 percent. Values of r less than 1.14 yield skin friction errors less than 2 percent.

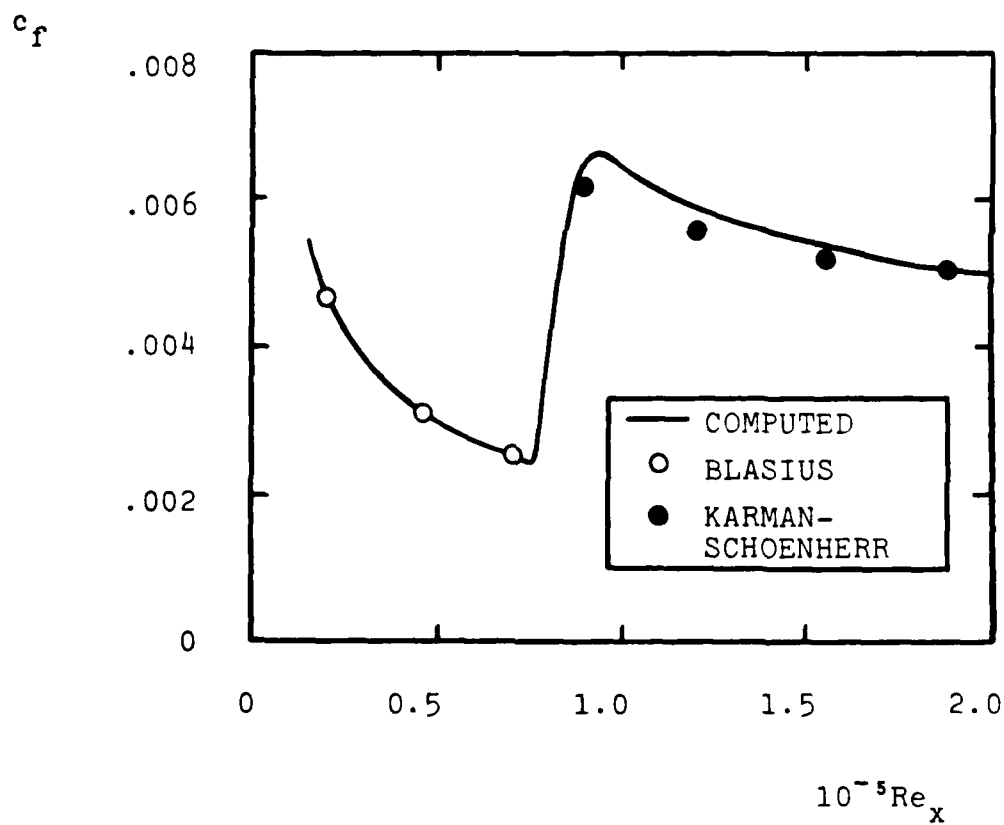
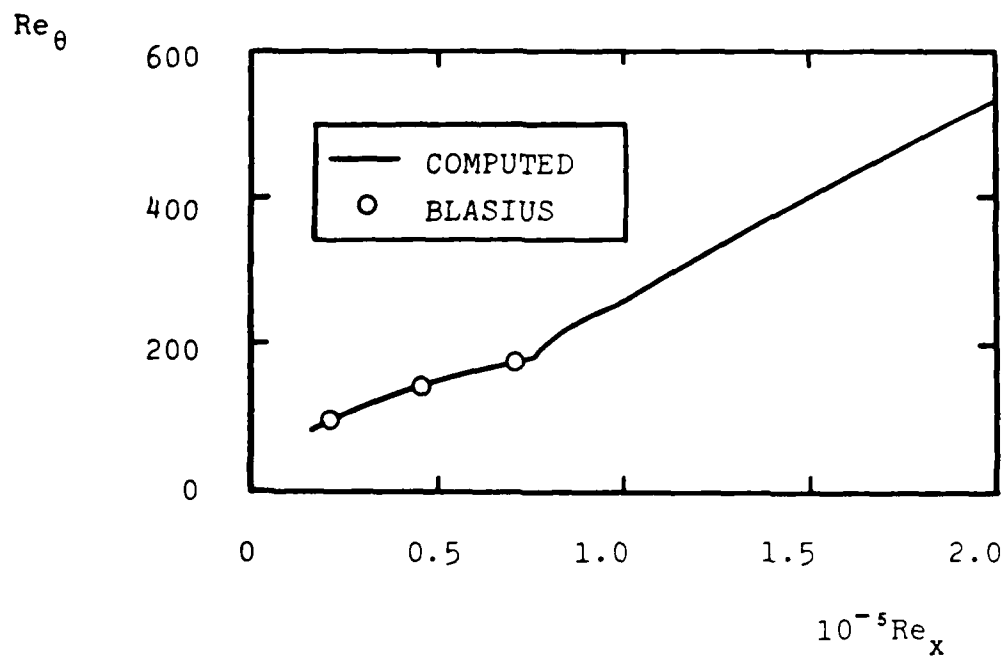


Figure 5. Comparison of computed and measured skin friction and momentum thickness for a transitional flat-plate boundary layer; 48 mesh points and $r = 1.11$.

PERCENT
ERROR
IN SKIN
FRICTION

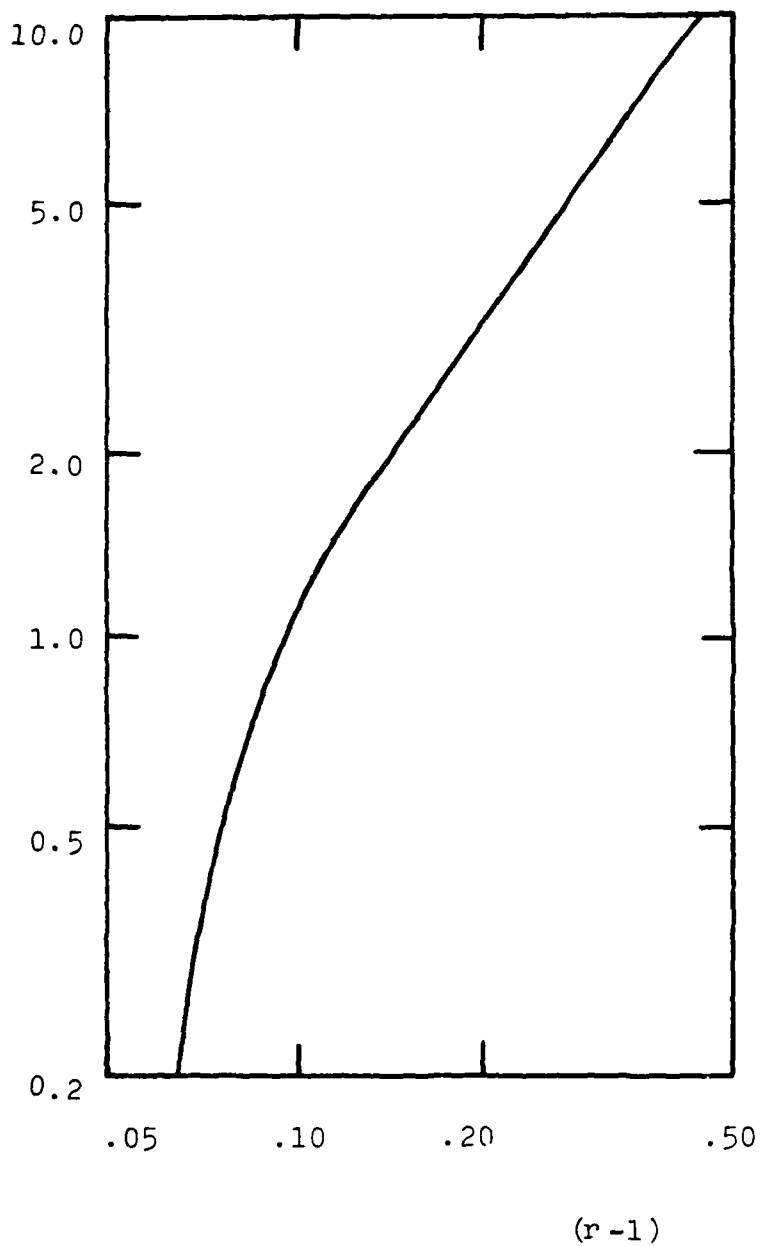


Figure 6. Variation of skin friction error with geometric progression grading ratio for a flat-plate boundary layer.

Figure 7 recasts the percent error in skin friction in terms of mesh point number. As shown, solutions are more or less mesh independent beyond about 60 mesh points.

PERCENT
ERROR
IN SKIN
FRICTION

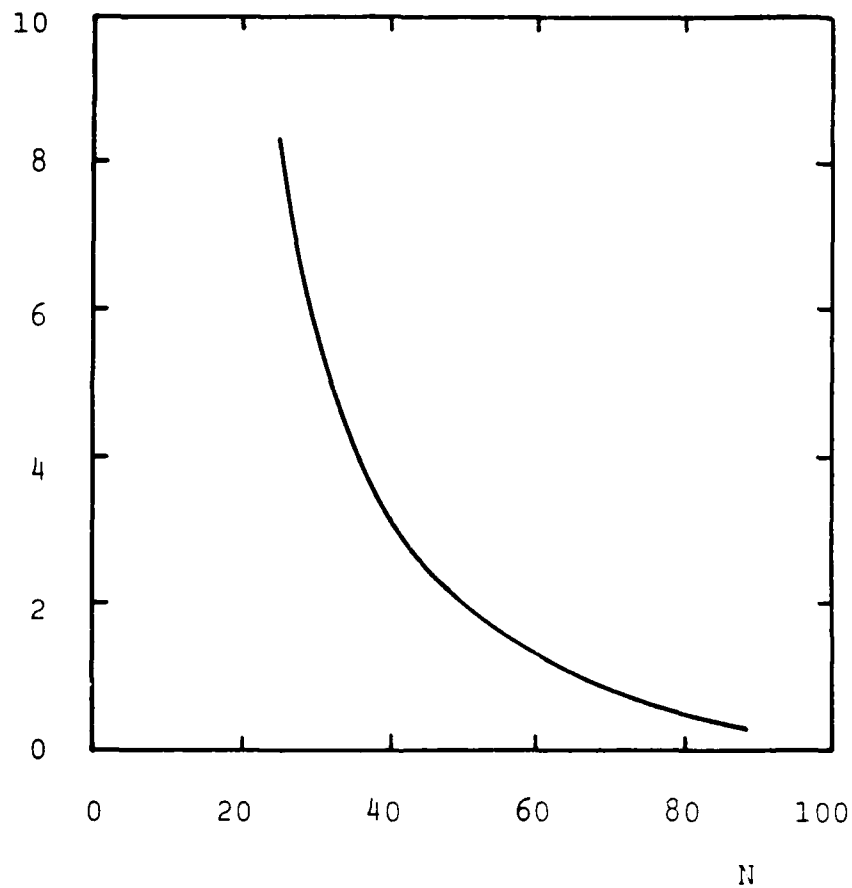


Figure 7. Variation of skin friction error with number of mesh points for a flat-plate boundary layer.

4. SHIP-HULL APPLICATIONS

We turn now to computation of the three-dimensional boundary layer on two ship hulls, viz, the SSPA Model 720 and the HSVA Tanker. These are the two test cases included in the 1980 SSPA-ITTC Workshop on ship boundary layers¹¹. For the SSPA Model 720 we perform three separate computations to test EDDY3's ability to handle reverse crossflow and sensitivity for grid point spacing. Then, the HSVA Tanker computation is done just once on an optimized grid.

The surface finite difference grid is nonorthogonal and PROGRAM SHPMESH (see Section A.1 of the Appendix) is used to generate the grid. Also, PROGRAM VELOC (see Section A.2 of the Appendix) is used to interpolate inviscid velocities onto the nonorthogonal grid.

4.1 SSPA MODEL 720

4.1.1 Effect of Girthwise Integration Direction

All of the computations performed use the Workshop-supplied Douglas-Neumann¹² inviscid velocity distribution. In all cases, computation is initiated from fully-turbulent boundary-layer profiles at $2x/L = -0.6$ (L is the hull half length). The profiles used match the measured momentum thickness and skin friction. For the computations of this Subsection, the finite-difference mesh consists of 51 equally-spaced points extending from $2x/L = -0.6$ to $2x/L = 0.9$, 11 equally-spaced points (in terms of girth) in the girthwise direction, and an average of 40 points normal to the surface. Thus, the mesh consists of about 22,000 points. Consistent with the Douglas-Neumann computation, both the keel line and the waterline have been treated as symmetry planes.

To further test the program's numerical formulation, we perform the computation in two different ways. First, we perform the girthwise integration starting at the keel and integrating toward the waterline on each streamwise plane (section). Then, we repeat the computation integrating from waterline to keel. Doing both

computations checks numerical-algorithm consistency and the program's ability to handle reverse crossflow.

Inspection of key flow properties shows virtually no difference between the two solutions through the entire flowfield. This confirms that the program is indeed able to handle reverse crossflow in a stable and accurate manner. It also confirms that overall the algorithm is consistent with the parabolic nature of the boundary-layer equations.

4.1.2 Effect of Mesh Refinement

In the next computation we use 81 mesh points in the streamwise direction, half of which lie between $2x/L = 0.5$ and $2x/L = 0.9$. A total of 21 equally-spaced points lie in the girthwise direction with an average of 75 points normal to the surface. This mesh consists of about 128,000 points, almost six times the number used in the computations of Subsection 4.1.1. The girthwise integration is carried out from keel to waterline.

A detailed comparison of corresponding flow properties for the 22,000- and the 128,000-mesh-point computations shows that overall flow properties differ by about 3 percent. Even in regions of rapid change, differences never exceed 5 percent. These observations are consistent with our accuracy study for the flat-plate boundary layer which indicate that, on the one hand, using 40 points normal to the surface yields a little over 3 percent error while, on the other hand, using 75 points results in about 0.6 percent error. The 5 percent discrepancies almost certainly attend the difference in streamwise resolution between the two computations.

Results of this numerical test indicate there is little point in using a mesh as fine as the one with 128,000 points if economy is a factor. That is, our 22,000-point computations require approximately 20 minutes on a UNIVAC 1108 while the 128,000-point computation requires about 90 minutes. Note that the increase

in machine time is slower than linear because use of the finer mesh is attended by fewer iterations in the solution procedure at each mesh point.

4.1.3 Comparison of Computed and Measured Momentum Thickness

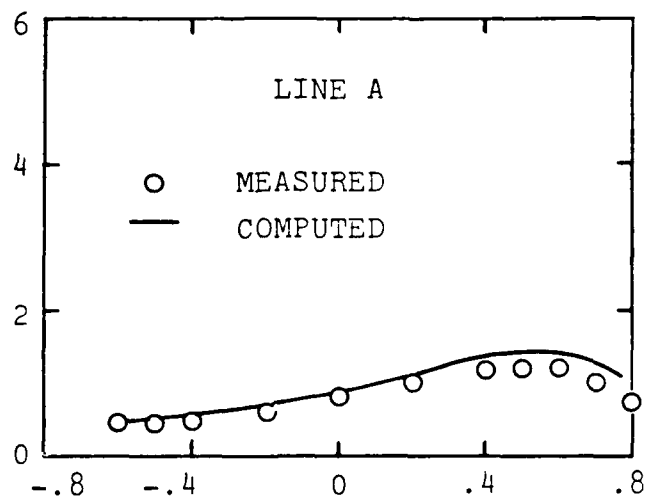
In all three computations, we predict boundary-layer separation over a portion of the hull beyond $2x/L = 0.77$. Although no separation appears to have been observed experimentally, one should also note that the experimentally observed boundary layers did not experience as strong an adverse pressure gradient as those predicted by the Douglas-Neumann computation.

Figure 8 compares computed and measured momentum thickness, θ , on three lines along the hull. Line A is the keel line. Line B is a line well below the waterline where the boundary layer is more-or-less of the classical "thin" variety. Line C is closer to the waterline and the boundary layer approaches the more complicated "thick" structure.

Along Line A, the boundary layer is truly three dimensional as exhibited by its curious behavior approaching the stern. Specifically, despite entering a region of adverse pressure gradient, the momentum thickness decreases. This behavior occurs because of large flow divergence near the stern. While the computed θ lies about 25 percent above measured values, note that our predicted curve is much closer to the data than those of virtually all Computers in the SSPA-ITTC Workshop on Ship Boundary Layers, most of whose curves were high by a factor of two!

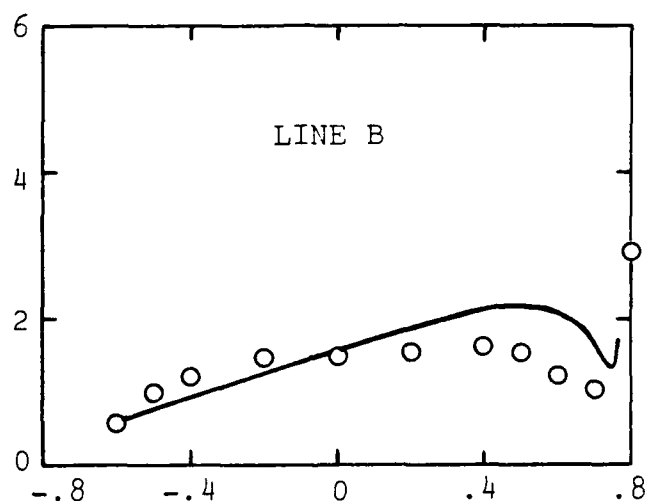
Along Line B, we exhibit somewhat larger differences from the measured values. Computers in the Conference generally came closest to experimental data on this line. Our prediction is about average relative to Conference participants'.

$$\frac{2\theta}{L} \cdot 10^3$$



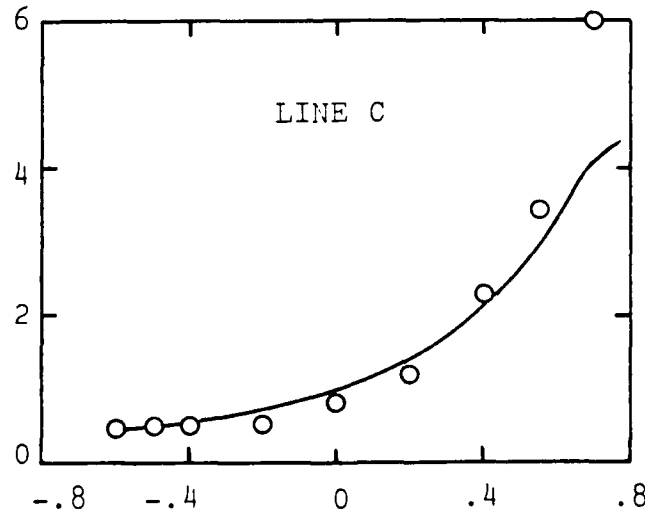
2x/L

$$\frac{2\theta}{L} \cdot 10^3$$



2x/L

$$\frac{2\theta}{L} \cdot 10^3$$



2x/L

Figure 8. Comparison of computed and measured momentum thickness for the SSPA Model 720.

On Line C, our predicted curve follows measured values quite closely up to about $2x/L = 0.5$; beyond this point we predict a slower-than-measured increase in momentum thickness. This is unsurprising as no provision has been made to accomodate any "thick" boundary-layer phenomena. Our prediction is much closer to the data than most Conference participants'.

4.2 HSVA TANKER

As with the SSPA Model 720, we use the Workshop-supplied Douglas-Neumann inviscid velocity distribution. Computation is initiated from fully-turbulent boundary-layer profiles at $2x/L = -0.80$. Again, the profiles used match the measured momentum thickness and skin friction. The finite-difference mesh consists of 70 points in the streamwise direction extending from $2x/L = -0.80$ to $2x/L = 0.90$, 15 equally-spaced points (in terms of girth) in the girthwise direction, and an average of 60 points normal to the surface. Figure 9 compares computed and measured momentum thickness on three sections, viz, for $2x/L = -0.744$, 0.291 and 0.502 . The numerical boundary layer separated over a substantial portion of the hull at $2x/L = 0.75$, so that comparison with momentum-thickness data at $2x/L = 0.884$ is not possible. Note that the abscissa, z , is the nondimensional girth with $z=0$ on the keel and $z=1$ on the waterline. Overall differences between computed and measured θ are similar to those obtained for the SSPA Model 720.

In summary, we have tested EDDY3 on two ship hulls and encountered no significant numerical difficulty. Separation on both hulls is almost certainly caused by the use of the Neumann inviscid velocities, so separation is discounted as a numerical problem. The differences observed between computed and measured momentum thickness, although generally much smaller than those of Workshop participants, are too large for general engineering applications. Thus, our predictive ability requires further improvement before a ship designer can apply a program such as EDDY3 with any degree of confidence.

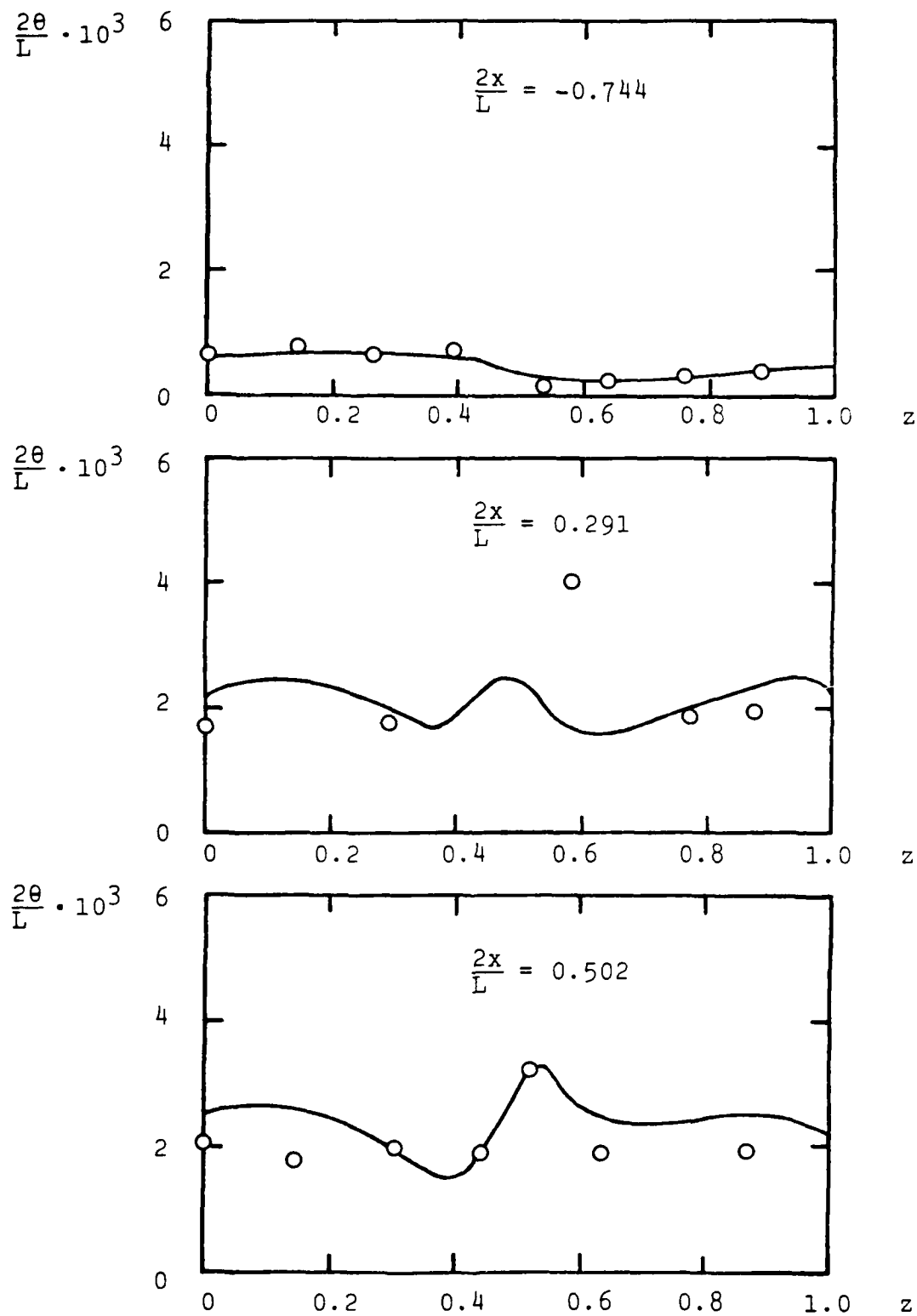


Figure 9. Comparison of computed and measured momentum thickness for the HSV A Tanker.

Inspection of Figures 8 and 9 indicates our predictions differ from measurements most significantly as we approach the stern. This is unsurprising because, on the one hand, we expect the boundary layer to become "thick" so that classical thin-shear-layer approximations become suspect while, on the other hand, our computations have been done with classical thin-shear-layer approximations. In the next section, we address the question of how well our model equations predict properties of "thick" boundary layers if we abandon the thin-shear-layer limit.

5. ANALYSIS OF THE THICK BOUNDARY LAYER

In this section we address the thick boundary layer by computing three axisymmetric flows in which boundary-layer thickness becomes large relative to the body radius. First we use perturbation methods to show that model equation solutions are consistent with the Rao and Richmond scaling laws for axisymmetric boundary layers. Then, we compute flow over a thin cylinder (wire) and compare computed and measured flow properties. Next, we compute flow over two axisymmetric bodies using both measured surface and boundary-layer-edge pressure distributions and deduce that including $\partial p / \partial y$ in a thick boundary layer computation will account for most of the observed differences from thin layers. Finally, we devise an integral method for computing $\partial p / \partial y$ in a thick axisymmetric boundary layer.

5.1 PERTURBATION ANALYSIS

The two most noteworthy scaling schemes for axisymmetric boundary layers are those of Rao¹³ and Richmond¹⁴. In Subsections 5.1.1 and 5.1.2 we use perturbation methods to show that the Wilcox-Rubesin model is consistent with Rao's scaling in the viscous sublayer and with Richmond's scaling in the wall layer.

5.1.1 Sublayer Scaling

For an axisymmetric boundary layer with constant pressure, close to the surface the Wilcox-Rubesin model simplifies to:

$$r(v + \gamma^* \epsilon) \frac{du}{dr} = r_0 u_\tau^2 \quad (19)$$

$$\frac{1}{r} \frac{d}{dr} \left[(v + \sigma^* \epsilon) r \frac{dk}{dr} \right] = \gamma^* \epsilon \left(\frac{du}{dr} \right)^2 - \beta^* \omega k \quad (20)$$

$$\frac{1}{r} \frac{d}{dr} \left[(v + \sigma \epsilon) r \frac{d\omega^2}{dr} \right] = \gamma \omega \left(\frac{du}{dr} \right)^2 - \left[\beta + 2\sigma \left(\frac{d\ell}{dr} \right)^2 \right] \omega^3 \quad (21)$$

where v and ϵ denote molecular and eddy diffusivity, r is radial distance, u is velocity, r_0 is body radius and u_τ is friction velocity.

Deep in the sublayer, the eddy viscosity can be neglected, i.e., $\epsilon \ll \nu$. Then, if we nondimensionalize according to:

$$\left. \begin{aligned} K &= k/u_{\tau}^2 \\ W &= \nu \omega / u_{\tau}^2 \\ L &= u_{\tau} \ell / \nu \\ r_o^+ &= u_{\tau} r_o / \nu \\ Y &= r_o^+ \log (r/r_o) \end{aligned} \right\} \quad (22)$$

substituting Equations (22) into Equations (19-21) yields

$$dU/dY = 1 \quad (23)$$

$$d^2K/dY^2 = \gamma^* K/W - \beta^* W K \exp(2Y/r_o^+) \quad (24)$$

$$d^2W^2/dY^2 = \gamma W - \beta W^3 \exp(2Y/r_o^+) - 2\sigma (dL/dY)^2 W^3 \quad (25)$$

For the most experimental measurements made on flows of this type the non-dimensional radius, r_o^+ , is very large so that

$$\exp(2Y/r_o^+) = 1 + O(1/r_o^+) \quad (26)$$

Thus, in the limit $r_o^+ \gg 1$, just as in the two-dimensional case it is easily verified that the production terms, $\gamma^* K/W$ and γW , and the term in Equation(25) proportional to $(dL/dY)^2$ are negligible. The solution to Equations (23-25) is then trivially shown to be

$$\left. \begin{aligned} U &= Y \\ W &= 20/(\beta Y^2) \\ E &\sim Y^4 \end{aligned} \right\} \quad (27)$$

Writing the dimensional equivalents of Equations (27) yields the following:

$$\left. \begin{aligned}
 u/u_\tau &= r_o^+ \log(r/r_o) \\
 vw/u_\tau^2 &= 20v/\{8(\log \frac{r}{r_o})\}^2 \\
 k/u_\tau^2 &\sim (r_o^+ \log \frac{r}{r_o})^4
 \end{aligned} \right\} \quad (28)$$

The velocity profile predicted in Equations (28) is precisely that given by the Rao scaling. To test the limiting u/u_τ asymptotic form, we have examined results of a numerical computation for flow past a thin cylinder aligned axially with the freestream (complete details of the computation are given in Subsection 5.2). For the data summarized below in Table 1 we have $r_o^+ = 667.8$. As indicated, although the effect is small because of the large value of r_o^+ , the numerical u/u_τ agrees with the values predicted by the first of Equations (28) to three decimal places. Thus, the analysis is self consistent.

Table 1. Comparison of Computed & Predicted
Sublayer Velocity Profiles

$u_\tau y/v$	$r_o^+ \log(r/r_o)$	$(u/u_\tau)_{\text{Computed}}$
0.6056	0.6053	0.6054
1.235	1.234	1.234
1.889	1.886	1.886
2.568	2.563	2.563
3.274	3.266	3.266
4.007	3.995	3.995
4.769	4.752	4.752

5.1.2 Wall-Layer Scaling

We turn now to the wall layer, viz, the region sufficiently close to the surface for convective terms to remain negligible yet far enough that the molecular viscosity can be neglected relative to the eddy viscosity. This is the classical law-of the wall region for planar boundary layers. We again nondimensionalize according to Equations

(22) with the exception that our normal coordinate is redefined as follows.

$$Y = y^+(1 + y^+/r_0^+) \quad \text{where} \quad y = (r - r_0) \quad (29)$$

The wall layer is most conveniently analyzed by treating U as the dependent variable. Dropping molecular viscosity in Equations (19-21), the equations for the wall layer are:

$$(1 + 2Y/r_0^+) (K/W) dU/dY = 1 \quad (30)$$

$$\sigma^* d^2 K/dU^2 = \beta^* (1 + 2Y/r_0^+) K^2 - 1 \quad (31)$$

$$\sigma d^2 W^2/dU^2 = \beta (1 + 2Y/r_0^+) K W^2 - \gamma W^2/K + 2\sigma (dL/dU)^2 W^4/K \quad (32)$$

In the limit of very large r_0^+ these equations are identical to those for planar boundary layers. From Equation (31) there follows immediately:

$$E = 1/\sqrt{\beta^*} + O(1/r_0^+) \quad (33)$$

Substituting Equation (33) into Equation (32), the solution for W becomes (noting that the closure coefficients have been chosen to insure that $\gamma = \beta/\beta^* - 2\sigma\kappa^2/\sqrt{\beta^*}$ where κ is Karman's constant):

$$W = \frac{1}{\kappa\sqrt{\beta^*}} \exp(-\kappa U) \quad (34)$$

Finally, substituting Equations (33-34) into Equation (30) yields the velocity profile, viz,

$$U = \frac{1}{\kappa} \log Y + O(1/r_0^+) \quad (35)$$

or in dimensional form we have:

$$u/u_\tau = \frac{1}{\kappa} \log \tilde{y}^+ + \dots \quad (36)$$

where

$$\tilde{y}^+ = y^+(1 + y^+/2r_o^+) \quad (37.)$$

Equations (36-37) are precisely those of the Richmond scaling.

In Figure 1 we compare our numerical predictions for the thin clinder computation of the next subsection with Equations (36-37). In the comparison we have included Coles' wake component so that the complete velocity profile becomes:

$$u/u_\tau = \frac{1}{\kappa} \log \tilde{y}^+ + B + \frac{2\tilde{\pi}}{\kappa} \sin^2\left(\frac{\pi}{2} \frac{\tilde{y}^+}{\delta^+}\right) \quad (38)$$

where we use $\kappa = .41$, $B = 5.0$ and $\tilde{\pi} = -.14$. Note that the inferred wake strength $\tilde{\pi}$ of $-.14$ implies that the transverse curvature effect is similar to a favorable pressure gradient. This point is consistent with the observations of Patel¹⁵. The overall agreement between the numerical profile and Equation (38) verifies the perturbation analysis.

5.2 FLOW PAST A WIRE

In this subsection we present results of a numerical computation for flow past a "wire", viz, a thin cylinder aligned axially with the freestream. The case we have chosen is that experimentally investigated by Yu¹⁶ in which the Reynolds number based on cylinder radius is

$$Re_{r_o} = 15,250 \quad (39)$$

Unit Reynolds number for the flow is $1.83 \cdot 10^5$ and measurements were made between axial distances, x , from 2 feet to 8 feet. At $x = 8$ feet the ratio of boundary layer thickness to r_o is approximately 2 so that this flow includes a moderately "thick" boundary layer.

Computation was initiated at $x = 0$ from laminar starting conditions. The freestream turbulence intensity was adjusted to yield a match between computed and measured momentum thickness at $x = 2$ feet.

Figure 11 compares predicted boundary layer thickness, δ , momentum thickness, θ , shape factor, H , and skin friction, c_f , with corresponding measurements. The data shown for δ , θ , and H are the original

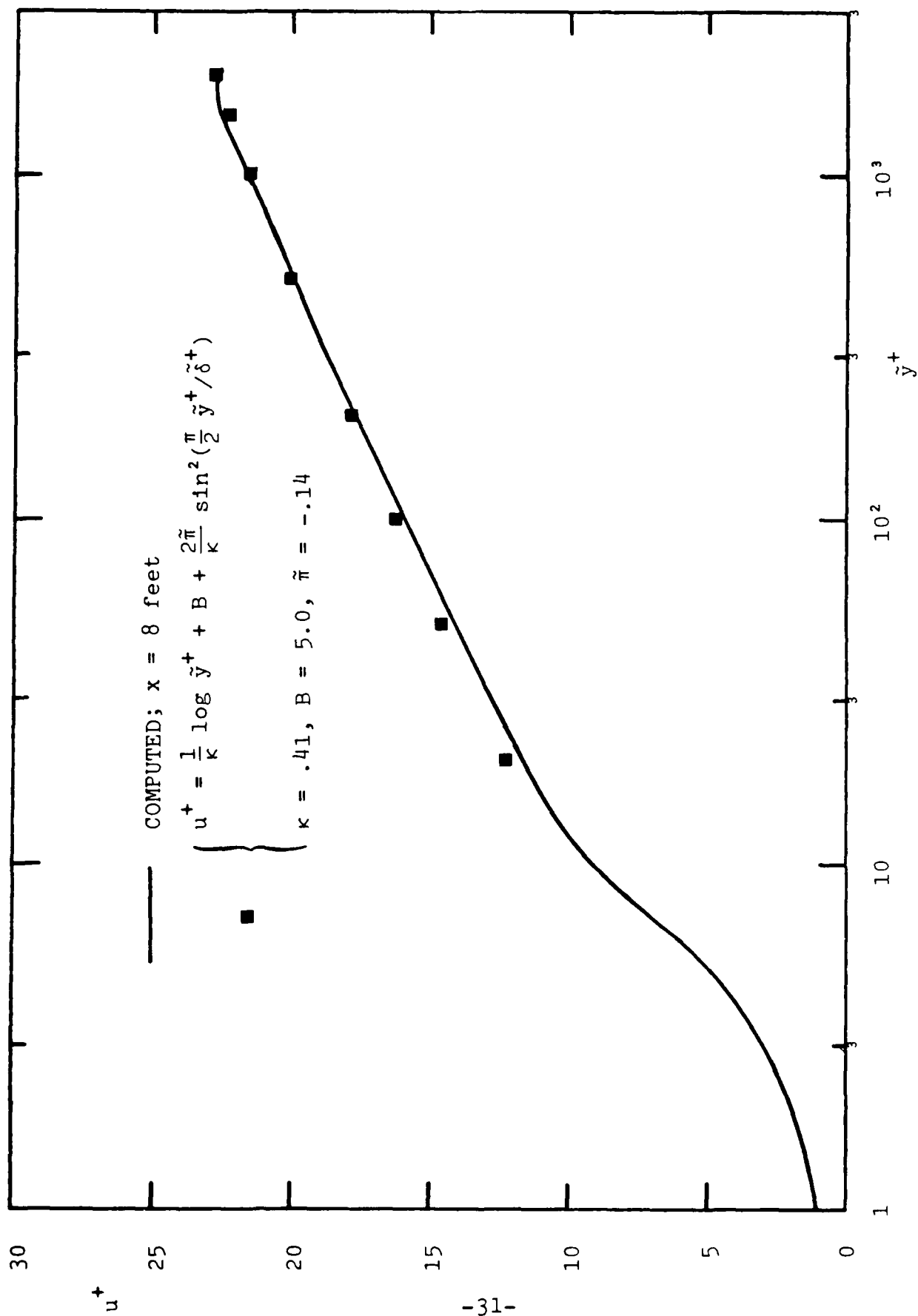


Figure 10. Comparison of a numerical velocity profile with that predicted by perturbation analysis of the Wilcox-Rubesin model.

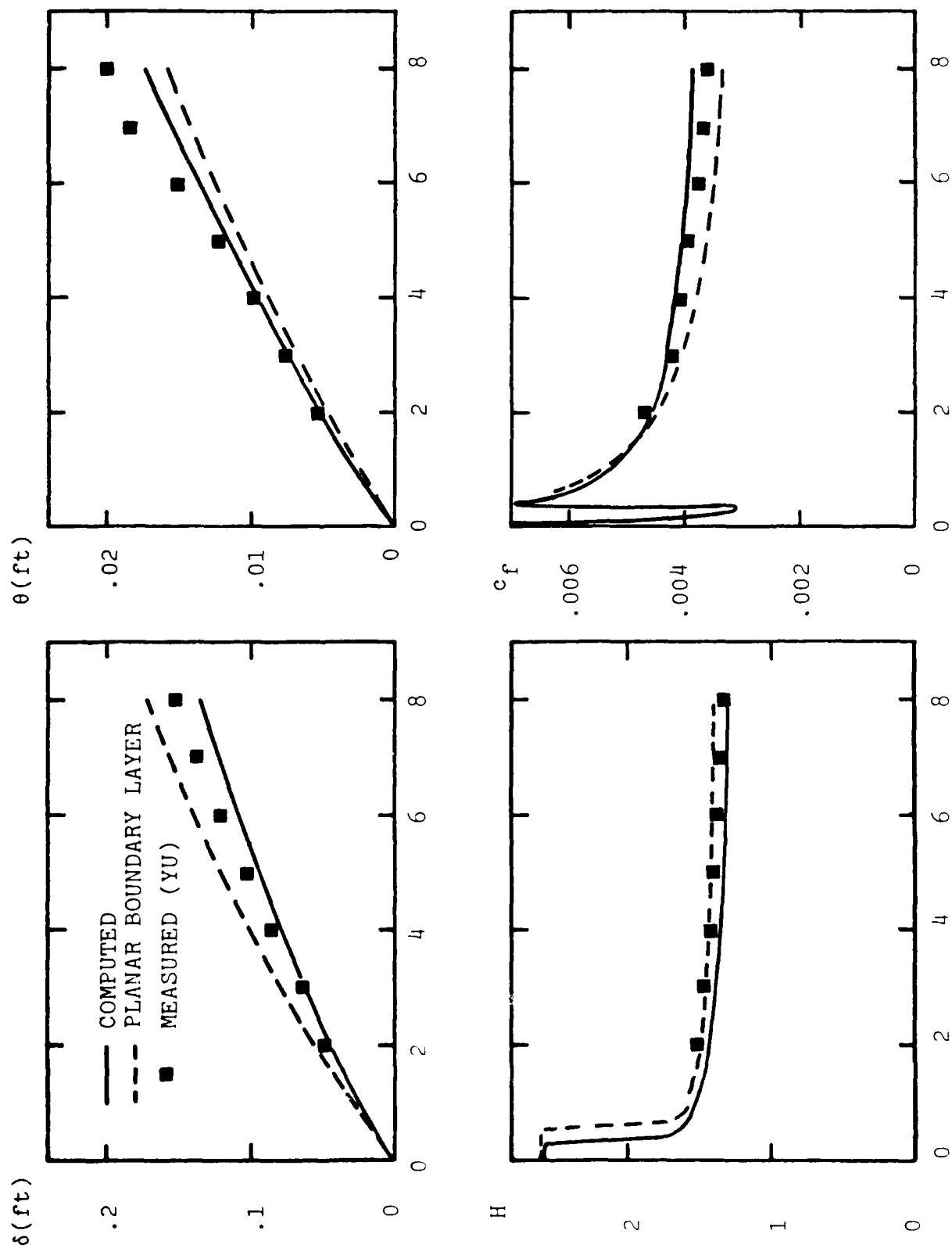


Figure 11. Comparison of computed and measured integral properties for flow past a thin cylinder aligned axially with the freestream; $Re_o = 15,250$.

data reported by Yu. The skin friction data have been obtained from Clauser plots rather than using Yu's Preston tube measurements which are thought to be in error¹⁵.

As shown, computed and measured shape factor and skin friction differ by less than 5%. Computed boundary-layer thickness is about 10% lower than measured while the numerical momentum thickness ultimately is about 15% lower than measured. The fact that our skin friction is so close to the measured values while the momentum thickness discrepancies are much larger leaves us with the same concern expressed by Patel¹⁷ regarding the two-dimensionality of the experimental flowfield. The figure also shows computed results for a corresponding planar boundary layer. As indicated, the primary effects of transverse curvature are to increase skin friction and momentum thickness and to decrease boundary-layer thickness and shape factor.

Figure 12 compares the computed and measured velocity profiles at the axial location $x = 8$ feet. With exception of the points lying between $y^+ = 150$ and 400, the computed velocity profile fares smoothly through the data. Even for the four data points lying between $y^+ = 150$ and 400, the maximum difference is less than 5%. Inspection of the profile for the corresponding planar case shows that the effect of transverse curvature is to alter the slope of the profile, a trend consistent with that displayed in the data.

Thus, for this constant-pressure flow, the model equations predict flow properties which are reasonably close to corresponding measurements. As will be seen in the next subsection, thick boundary layers experiencing an adverse pressure gradient cannot be as accurately computed if we restrict ourselves to classical thin-shear-layer approximations.

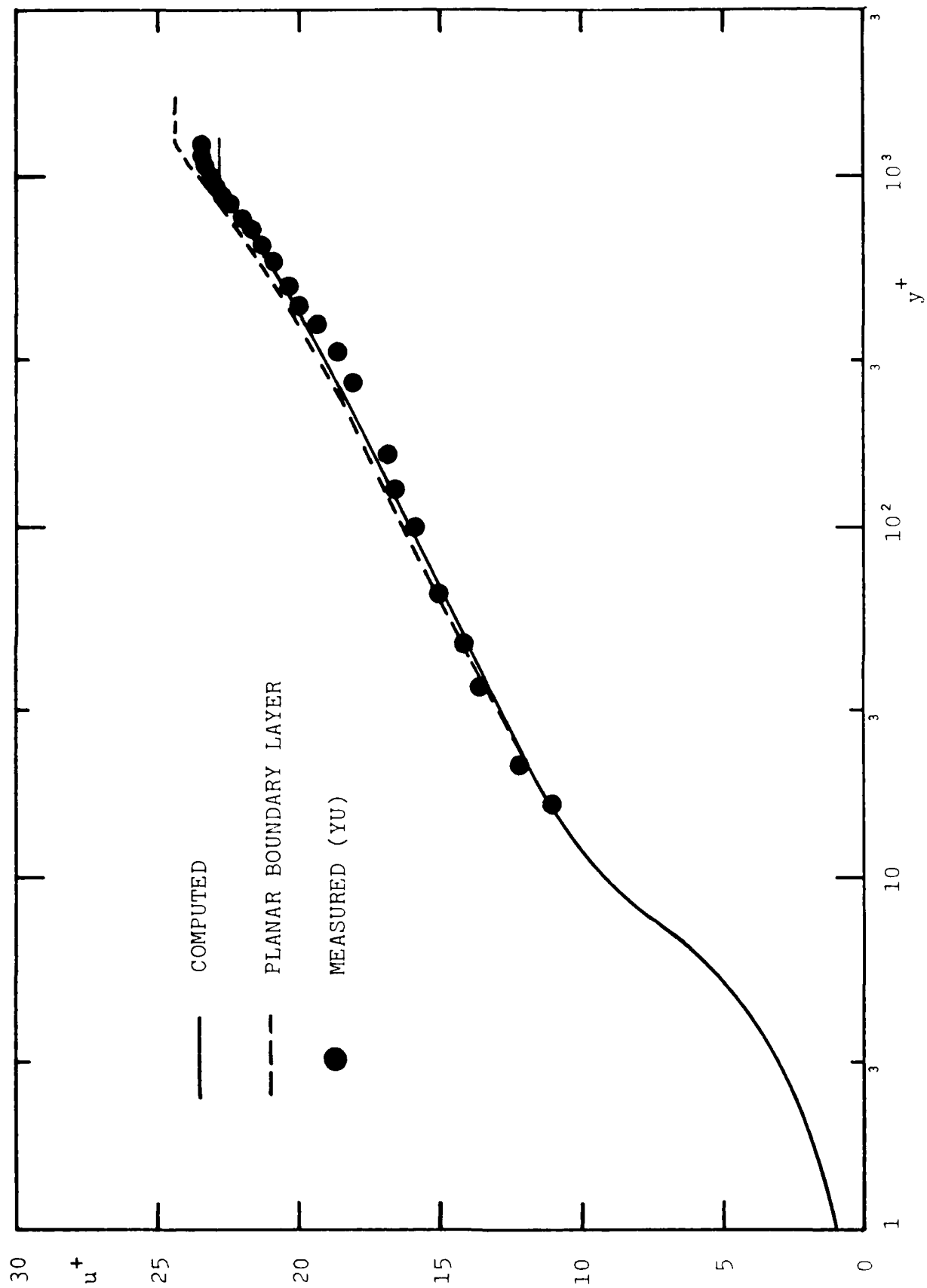


Figure 12. Comparison of computed and measured velocity profiles for flow past a thin cylinder aligned axially with the freestream; $Re_{r_0} = 15,250$, $x = 8$ feet.

5.3 BODIES WITH ADVERSE PRESSURE GRADIENT

In this Subsection, we make a "first cut" at two thick axisymmetric boundary layers with pressure gradient and streamline curvature. We emphasize that our computations are indeed only a first cut as experimental measurements indicate nontrivial variation in pressure across the boundary layers while we have used a standard boundary-layer program which assumes $\partial p / \partial y = 0$. In order to provide a first estimate of the importance of having variable pressure across the layer, we have done both computations first using the measured edge-pressure distribution and then with the measured surface-pressure distribution.

The two cases considered are the "modified spheroid"¹⁸ and the "low-drag body"¹⁹ experimentally evaluated by Patel. In Subsection 5.3.1 we compare computed and measured integral properties. Subsection 5.3.2 compares computed and measured velocity and Reynolds shear-stress profiles for the low-drag body. Next, in Subsection 5.3.3, we compare predicted peak eddy viscosity and mixing length with corresponding measurements. Finally, Subsection 5.3.4 examines the predicted effect of streamline curvature for the modified spheroid.

5.3.1 Integral Properties

Figures 13 and 14 compare computed and measured integral properties for the two axisymmetric bodies. Note that the modified spheroid computation has been initiated at $x/L = .662$ using the experimentally measured profiles to establish starting profiles. Reynolds number based on body length is $Re_L = 1.26 \cdot 10^6$. For the modified spheroid, boundary-layer thickness, δ , exceeds the body radius, r_0 , for all points beyond about $x/L = .925$. Similarly for the low-drag body, computation has been initiated at $x/L = .6$, again using the experimentally measured profiles for starting conditions. Reynolds number, Re_L , is $1.20 \cdot 10^6$ while δ exceeds r_0 beyond about $x/L = .85$.

Focusing first on the modified spheroid, note that the boundary layer

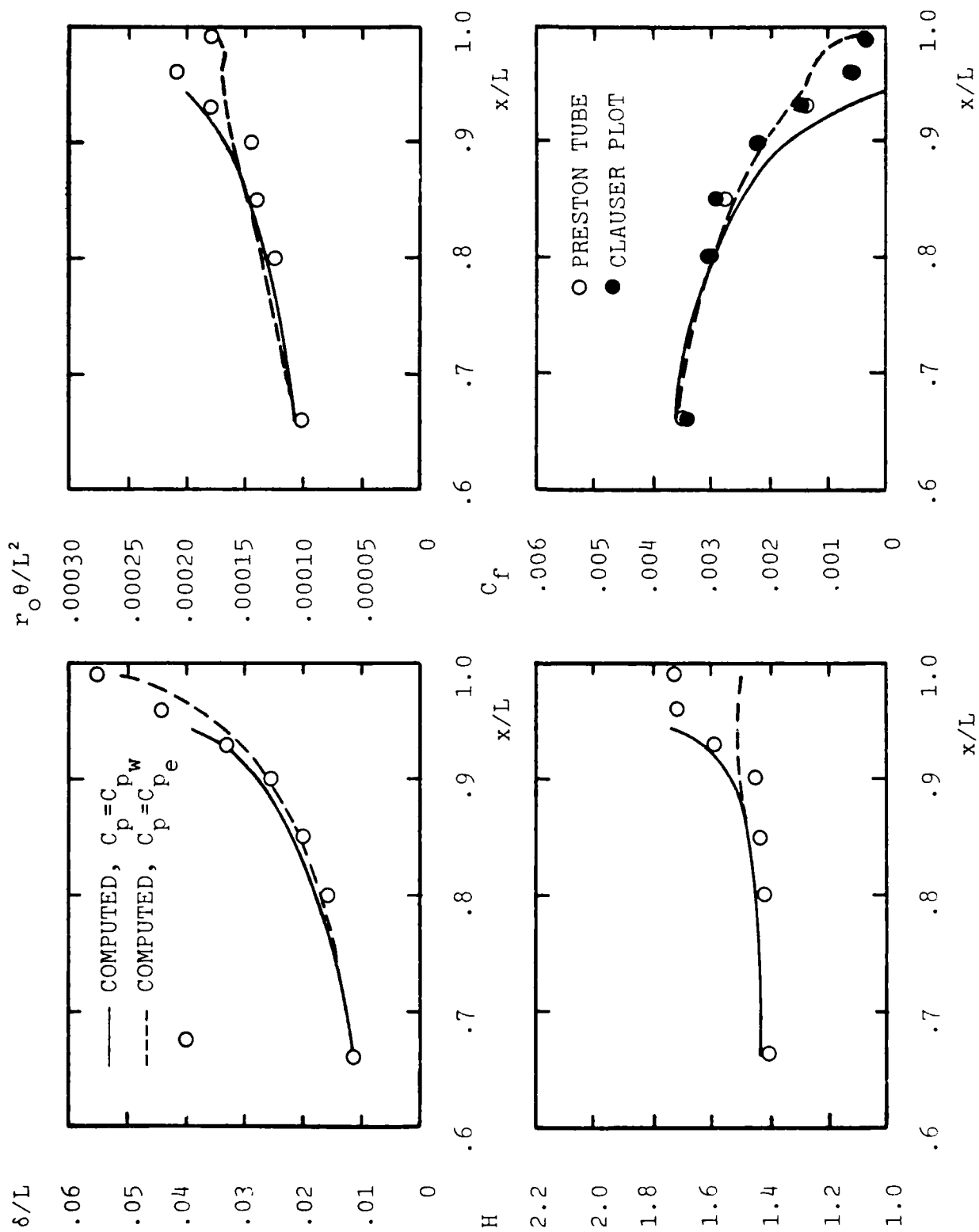


Figure 13. Comparison of computed and measured integral properties for Patel's modified spheriod; $Re_L = 1.26 \cdot 10^6$.

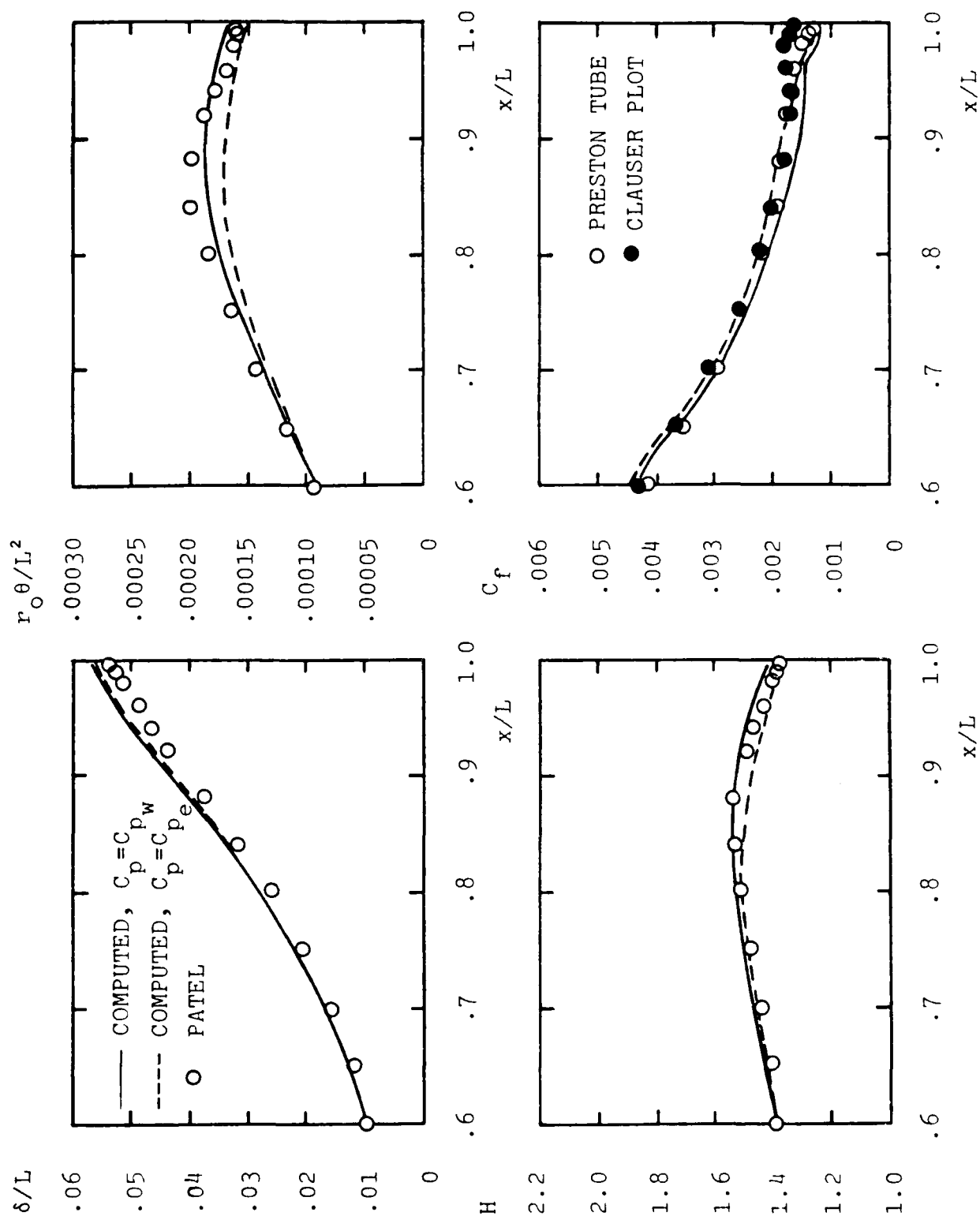


Figure 14. Comparison of computed and measured integral properties for Patel's low-drag body; $Re_L = 1.20 \cdot 10^6$.

remains attached to $x/L = .99$ when we use C_{pe} and separates at $x/L = .942$ when we use C_{pw} . For both pressure distributions, the predicted growth of the boundary-layer thickness is reasonably close to the measured trend with the experimental data beyond $x/L = .9$ lying between the two computed curves. Similarly, the experimental skin-friction, C_f , data tend to fall between the C_{pe} and C_{pw} curves, particularly in the region beyond $x/L = .9$ where $\partial p/\partial y$ is known from measurements to be nontrivial. On balance, the C_{pw} computation predicts momentum-thickness, θ , and shape-factor, H , distributions which are closer to the corresponding measurements in the interesting (i.e., $x/L > .9$) portion of the flow.

Turning now to Patel's low-drag body, note that the experiment was designed to avoid any complications attending incipient separation, such as that observed for the modified spheroid. As shown in Figure 14 neither computation predicts separation and differences between the two computations are less dramatic than in the modified spheroid case. As with the preceding computation, predicted overall growth of the boundary-layer thickness is quite close to the measured growth. For both computations, computed and measured C_f differ by less than 12%. As with the modified spheroid, differences between computed and measured θ and H distributions are smallest for the C_{pw} computation.

In summary, comparison of predicted and measured integral properties indicates that the experimental δ and C_f fall between the limiting C_{pe} and C_{pw} computations. Predicted θ and H distributions are closest to the corresponding measurements when we use $C_p = C_{pw}$. Hence, it appears that in taking a closer look at our predictions, the C_{pw} computations will provide more insight than those using C_{pe} .

5.3.2 Velocity and Reynolds-Stress Profiles

Because the modified spheroid computation separates, there is little positive information to be gleaned from detailed comparison of computed and measured profiles. Hence, in this Subsection, we focus our attention on the low-drag body.

Figure 15 compares computed and measured velocity profiles at four axial

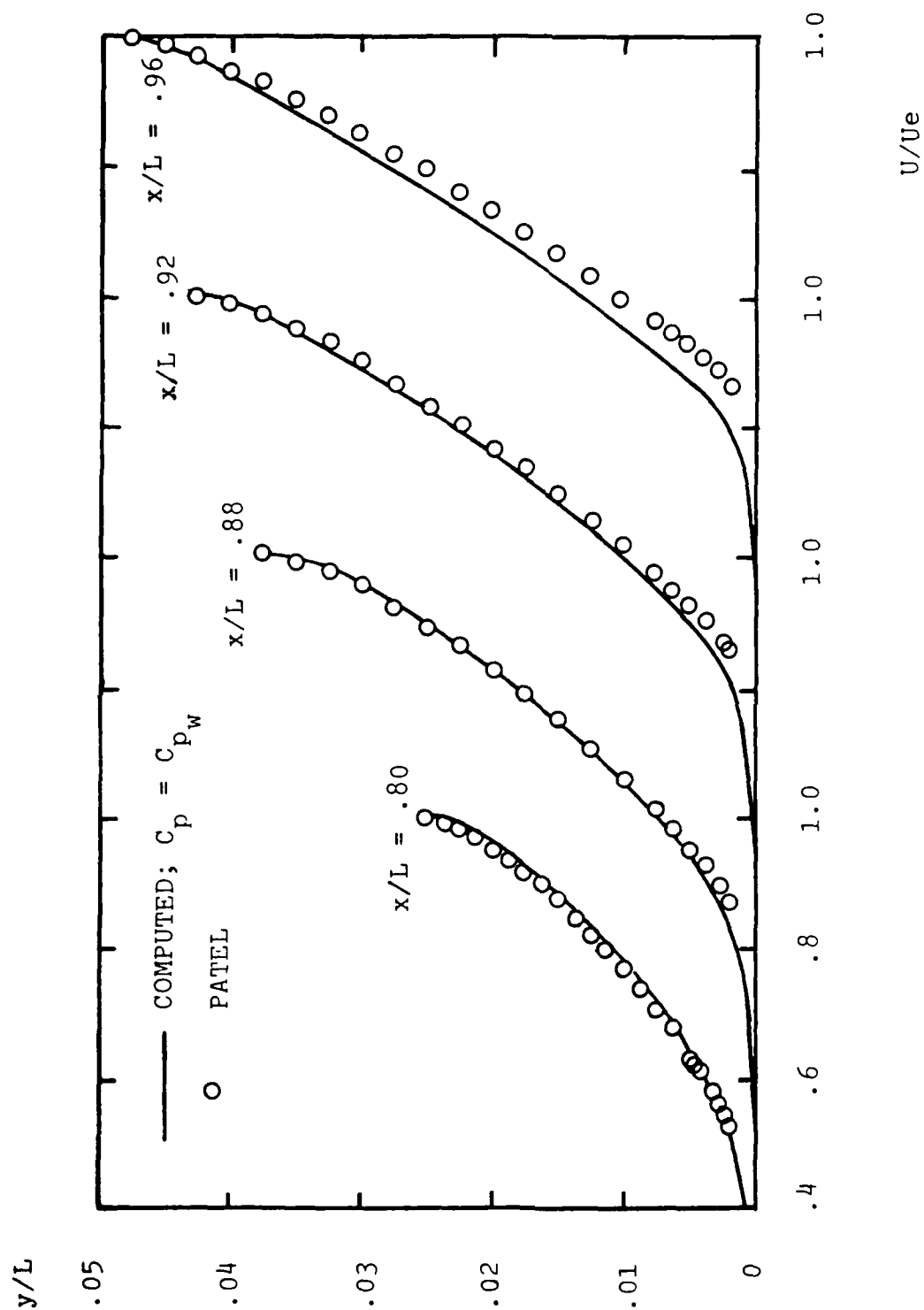


Figure 15. Comparison of computed and measured velocity profiles for Patel's low-drag body; $Re_L = 1.20 \cdot 10^6$.

stations, viz, $x/L = .80, .88, .92, .96$. As shown, the computed boundary layer has experienced stronger deceleration than in the experimental case. This is unsurprising as we have used the surface-pressure distribution throughout the layer which is attended by a larger gradient. Clearly, the overall growth matches that measured. Even at $x/L = .96$, differences between computed and measured velocities are less than 7% of scale.

Figure 16 compares computed and measured Reynolds shear-stress profiles. Discrepancies between the profiles at $x/L = .80$ are surprising, particularly in the light of the close agreement between the velocity profiles at this station. Overall, the numerical shear-stress profiles are within about 15% of scale of the measured profiles. The shapes and fullness of the experimental profiles are reasonably well simulated throughout the tail region of the body.

5.3.3 Turbulence Properties

In this subsection we concentrate on two key features of the turbulence field which have not been accurately simulated with simpler turbulence models. Specifically, we examine the variation of peak mixing-length, ℓ_{\max} , and eddy viscosity, ϵ_{\max} . Figure 17 compares our C_{pw} predictions with values inferred from Patel's data. As shown, for both bodies, model-predicted ℓ_{\max} and ϵ_{\max} fall off rapidly as we approach the tail of the body. Considering the inaccuracies attending differentiation of the experimental data required to infer ℓ_{\max} and ϵ_{\max} , our predictions must be considered well within the error band of the data.

5.3.4 Streamline-Curvature Effects

To obtain an estimate of the effects of streamline curvature on our predictions, we have rerun the C_{pw} modified-spheroid computation without account for streamline curvature. All results presented in Subsections 5.3.1-5.3.3 include the Wilcox-Chambers²⁰ curvature modification to the turbulent mixing-energy equation. Figure 18 shows effects on the velocity profile at $x/L = .93$. For the computation with no curvature, the numerical profile passes through all of the measured points. With curvature included, the velocity profile shows additional deceleration, consistent with the effect of convex curvature. Note

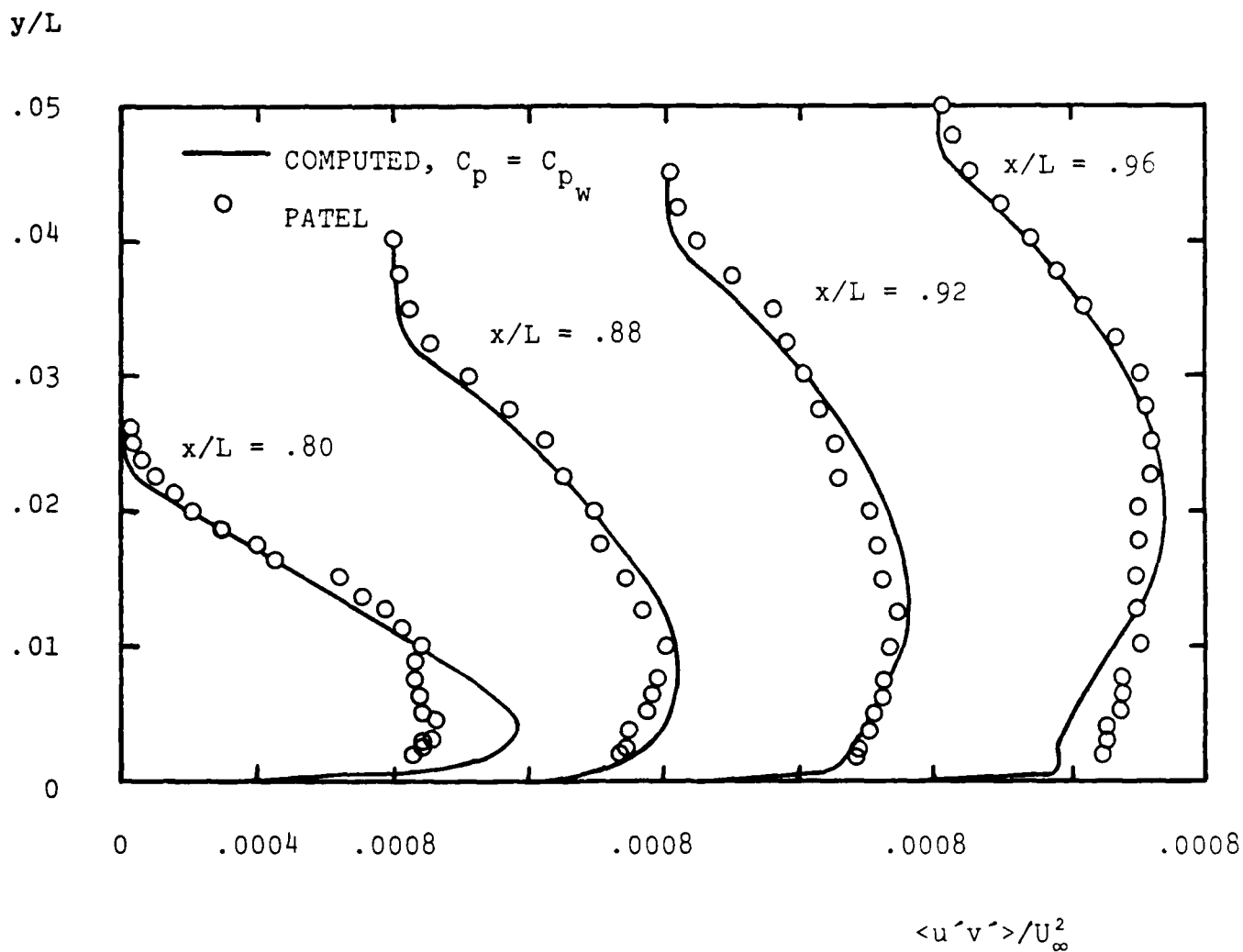


Figure 16. Comparison of computed and measured Reynolds shear-stress profiles for Patel's low-drag body; $Re_L = 1.20 \cdot 10^6$.

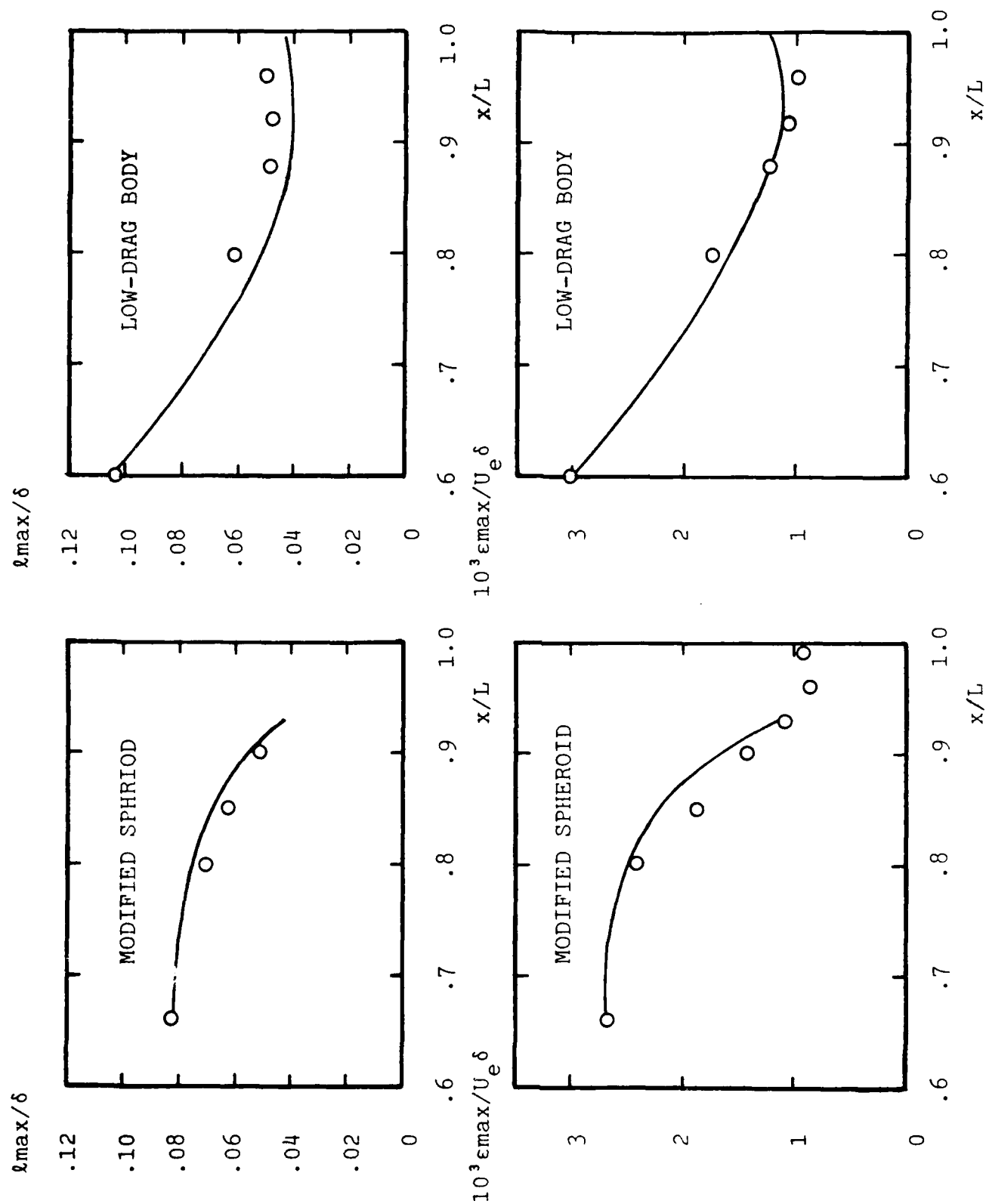


Figure 17. Comparison of computed and measured peak mixing-length and eddy-viscosity distributions; $C_p = C_{pw}$.

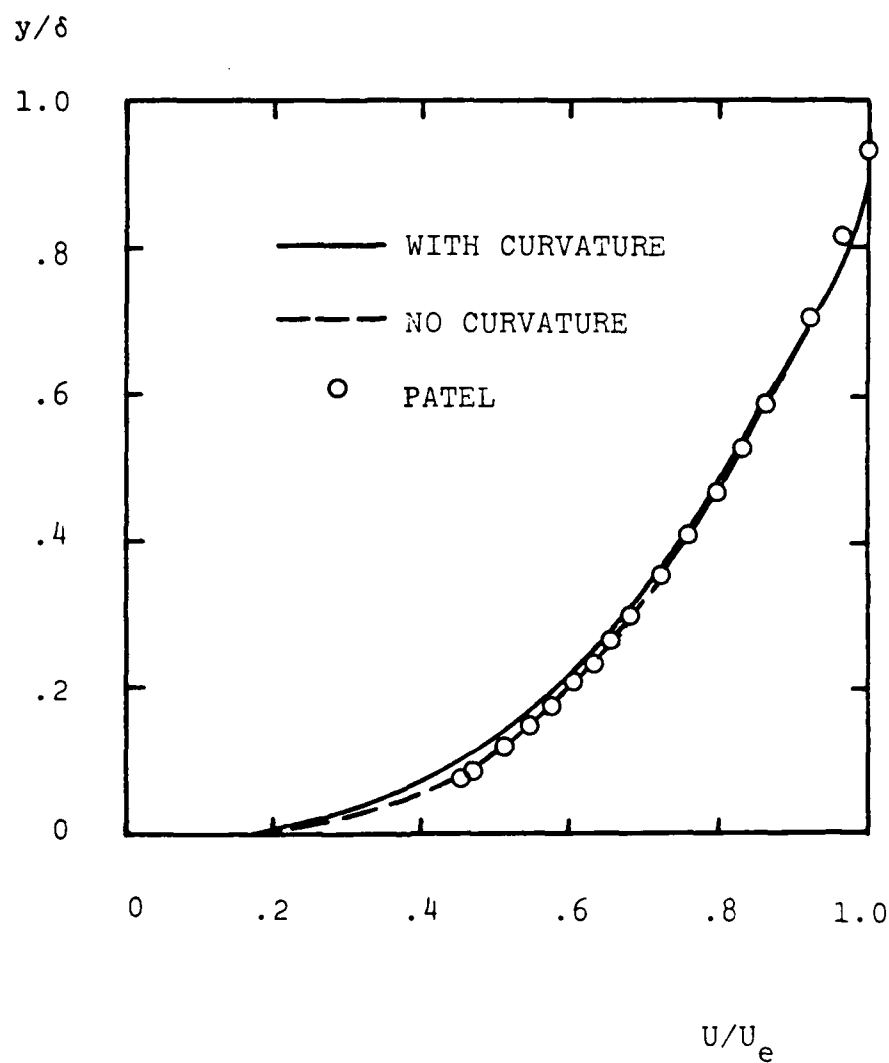


Figure 18. Predicted effect of streamline curvature for Patel's modified spheroid; $C_p = C_{pw}$ and $x/L = .93$.

that the close agreement between results of the no-curvature computation and the experimental data is fortuitous as the numerical pressure gradient is larger through much of the boundary layer than it is in the experimental case. Overall, the effect of curvature for the modified spheroid is small, giving rise to changes in integral properties of less than 5%

In summary, results of these two computations indicate the following.

1. With no modifications to the Wilcox-Rubesin turbulence model, computed boundary-layer thickness virtually duplicates measured thickness for both bodies.
2. Performing the computations with first the measured boundary-layer-edge pressure distribution and then with the measured surface pressure distribution (neglecting pressure variation across the layer in each computation) yields skin-friction distributions which overall fall above and below measured skin friction, respectively.
3. Shape factor and momentum thickness are in closer agreement with corresponding measurements when the wall pressure is used.
4. For one of the two bodies, our predictions suggest that streamline curvature plays a relatively minor role.

Thus, we conclude that the primary differences between the "thick" and the "thin" boundary layer are primarily caused by the pressure gradient across the former, i.e., $\partial p / \partial y$. In the next Subsection, we devise a straightforward method for including $\partial p / \partial y$ in a standard boundary-layer computation.

5.4 PRESSURE VARIATION IN A THICK BOUNDARY LAYER

Results of the preceding Subsection demonstrate the importance of pressure variations across a thick axisymmetric boundary layer. Recapitulating, we found that in using a conventional boundary

layer program, results obtained differ depending upon the pressure distribution used. On the one hand, using the measured freestream pressure distribution tends to underpredict momentum thickness and to overpredict skin friction. On the other hand, using the measured surface pressure tends to reverse the situation with momentum thickness overpredicted and skin friction underpredicted. Presumably, permitting the pressure to vary across the layer will yield numerical predictions which fall somewhere between these two limits. Because the experimental data lie between these two limits, predictions should then lie quite close to corresponding measurements. The object of this Subsection is to devise a method, compatible with a conventional boundary-layer marching algorithm, for predicting the pressure variation through a thick boundary layer.

In order to account for nonzero $\partial p / \partial y$ in a boundary layer, we must, in principle, solve the vertical as well as the streamwise momentum equation. For a thick boundary layer on a surface with curvature κ , Patel²¹ has shown that the vertical momentum and continuity equations are:

$$u \partial v / \partial x + h v \partial v / \partial y - \kappa u^2 + \frac{h}{\rho} \partial p / \partial y = 0 \quad (40)$$

$$\partial(ru) / \partial x + \partial(rh v) / \partial y = 0 \quad (41)$$

where u and v denote streamwise and vertical velocity components, x and y are streamwise and normal distances, ρ is density, p is pressure, r is radial distance, and h is the metric defined by

$$h = 1 + \kappa y \quad (42)$$

The curvature, κ , is understood to be positive for convex surfaces and negative for concave surfaces.

One approach to solving for the pressure would be to discretize Equation (40) and solve for p once v is known from the standard boundary-layer solution. This is not very convenient when the program is formulated in terms of Levy-Lees variables, however, and all of our programs use these variables. As an alternative, we have

chosen to implement an integral solution approach. Proceeding in the classical manner, we define the following boundary-layer thickness parameters:

$$\text{Displacement Thickness} \dots r\delta^* = \int_0^\delta (1-u/u_e) r dy \quad (43)$$

$$\text{U-Momentum Thickness} \dots r\theta = \int_0^\delta \frac{u}{u_e} (1-u/u_e) r dy \quad (44)$$

$$\text{V-Momentum Thickness} \dots r\theta_v = \int_0^\delta \frac{u}{u_e} (1-v/v_e) r dy \quad (45)$$

where δ is the boundary-layer thickness. Then, introducing the following quantities:

$$r_e = r_o + \delta \cos \phi, \quad h_e = 1 + \kappa \delta, \quad r_o \delta_r = \int_0^\delta r dy \quad (46)$$

the integral form of Equations (40-41) is as follows.

$$r_e [h_e v_e - u_e d\delta/dx] + d[r_o(\delta_r - \delta^*) u_e]/dx = 0 \quad (47)$$

$$\begin{aligned} d[r_o u_e v_e \theta_v]/dx - r_o(\delta_r - \delta^*) u_e dv_e/dx + \kappa r_o u_e^2 (\delta_r - \delta^* - \theta) \\ = \int_0^\delta \frac{h}{p} (\partial p / \partial y) r dy \end{aligned} \quad (48)$$

In order to make further headway we must postulate profiles for v and p . Close examination of data for two thick axisymmetric bodies^{18,19} shows that at all stations for which data were tabulated, both v and p can be closely approximated with simple linear profiles, viz,

$$v = v_e (y/\delta) \quad \text{and} \quad p = p_e + (p_w - p_e) (1-y/\delta) \quad (49)$$

Thus, the definition of θ_v is altered in the obvious way while Equation (48) simplifies to:

$$\begin{aligned} d[r_o u_e v_e \theta_v]/dx - r_o(\delta_r - \delta^*) u_e dv_e/dx + \kappa r_o u_e^2 (\delta_r - \delta^* - \theta) \\ = (r_o U_\infty^2 / 2\delta) \left[\delta_r + \frac{2}{3} \kappa \delta (\delta_r - \delta/4) \right] (C_{p_e} - C_{p_w}) \end{aligned} \quad (50)$$

In order to test this formulation, we have applied Equations (47 and 50) to three flows, in each case working with measured flow properties. The three cases are Yu's¹⁶ flow over a wire, Patel's modified spheroid¹⁸ and Patel's low-drag body¹⁹, respectively. For Yu's wire flow, we find that the difference between edge and surface pressure coefficients is of order 10^{-4} , as would be expected for this constant pressure case. Figures 19 and 20 compare predicted and measured pressure coefficient difference for the two Patel bodies. Considering the numerical crudeness attending differentiation of the data, particularly v_e , the agreement between the predictions of Equation (50) and the measured C_p difference is excellent.

Note that Equations 47 and 50 are not restricted to axisymmetric boundary layers. The limiting two-dimensional forms follow by formally replacing r_e by r_o and δ_r by δ . The equations can be generalized in a straightforward manner for three-dimensional boundary layers.

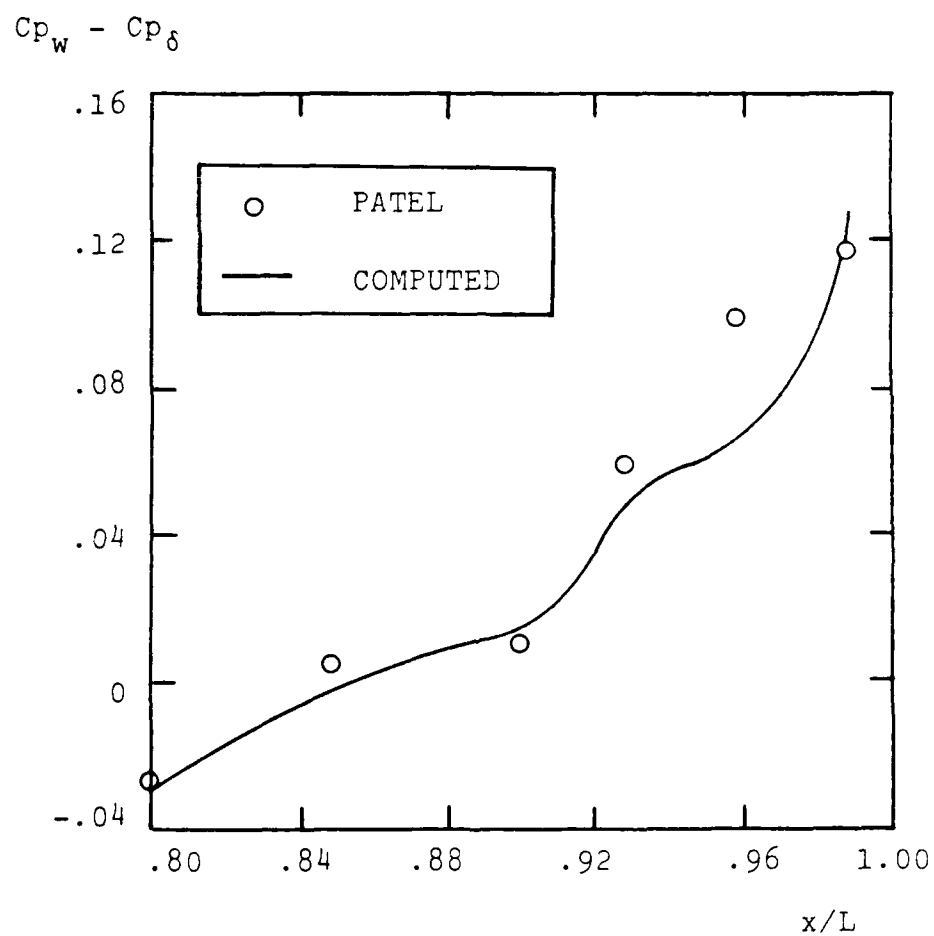


Figure 19. Comparison of predicted and measured pressure differential for Patel's modified spheroid.

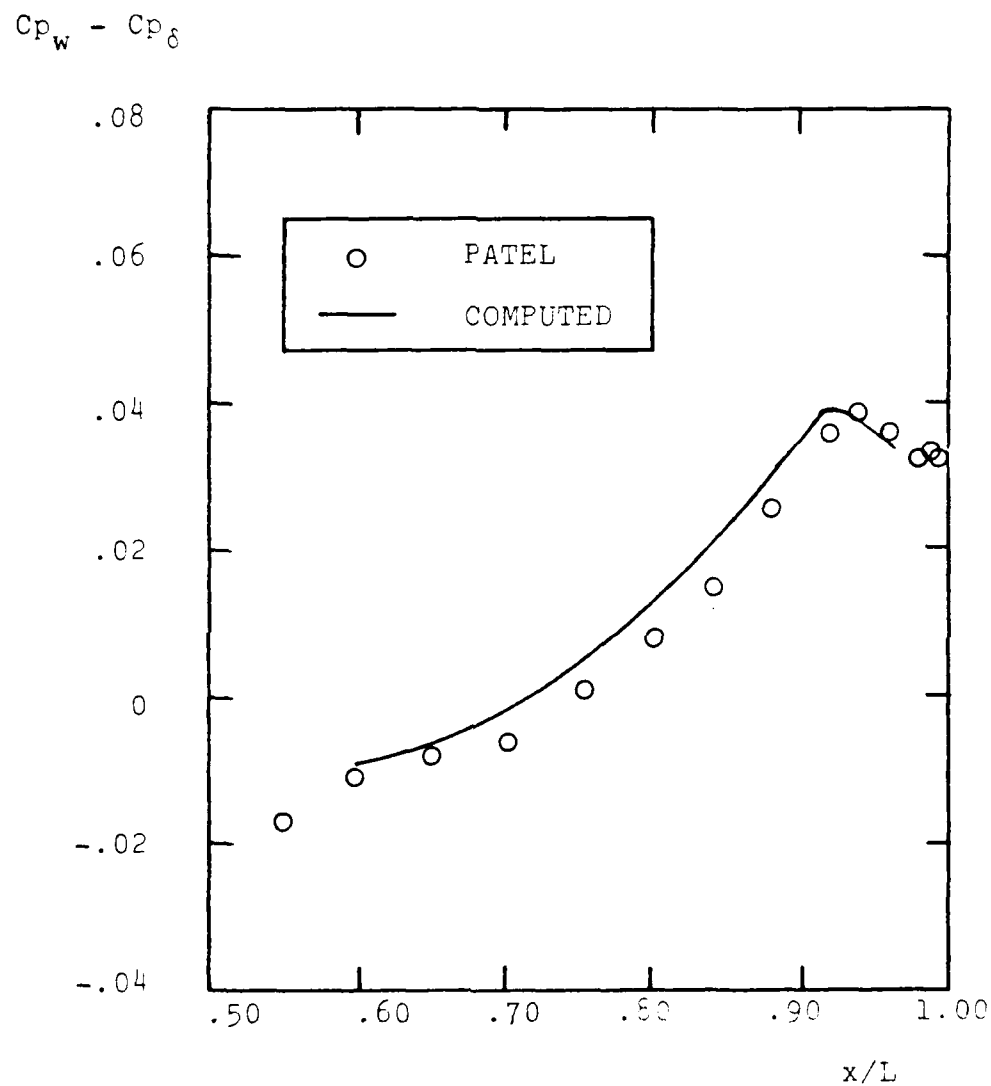


Figure 20. Comparison of predicted and measured pressure differential for Patel's low-drag body.

6. DISCUSSION

We have developed a new three-dimensional boundary-layer program, EDDY3, suitable for application to arbitrary ship hulls. The program embodies the Wilcox-Rubesin two-equation turbulence model and uses an accurate, efficient numerical procedure based on the Elotner "variable-grid" method coupled with the Krause explicit marching algorithm.

Results described in Sections 3 and 4 show that very accurate numerical results can be obtained with relatively coarse finite-difference grids. Computing times are quite modest as a complete ship hull computation can be done with about a half-hour of UNIVAC 1108 execution time. This corresponds to approximately three minutes on a CDC 7600 computer. Additionally, the numerical algorithm displays no noticeable difficulty when reverse crossflow is present.

Comparison of computed and measured flow properties for the SSPA Model 720 and the HSVA Tanker show that, on the one hand, our predictions are quite a bit closer to measurements than those reported in the 1980 SSPA-ITTC Workshop on Ship Boundary Layers. On the other hand, differences are too large, particularly near the ship stern, for us to claim the problem is solved. The fact that the boundary layer becomes "thick" approaching the stern is no doubt the cause of the differences observed between theory and experiment.

Our analysis of thick axisymmetric boundary layers in Section 5 shows that, in order to obtain accurate "thick" boundary-layer predictions, accounting for the normal pressure gradient, $\partial p / \partial y$, probably is all that is needed above and beyond conventional thin-shear-layer approximations. Streamline curvature variation appears to play a relatively minor role in the "thick" boundary layer.

Additional research is needed to confirm the importance of $\partial p / \partial y$ in ship-hull computations. The formalism developed in Subsection 5.4

can be easily generalized for a 3-D boundary layer and should be included in EDDY3. We could then repeat the two ship-hull computations of Section 4 to confirm our hypothesis. Additionally, it would be instructive to use measured freestream flow conditions in the computations.

REFERENCES

1. MacCormack, R.W., "A Numerical Method for Solving the Equations of Compressible Viscous Flow," AIAA Paper 81-0110 (1981).
2. Wilcox, D.C., "Numerical Study of Separated Turbulent Flows," AIAA Journal, Vol 13, No 5, pp 555-556 (1975).
3. Wilcox, D.C. and Rubesin, M.W., "Progress in Turbulence Modeling for Complex Flow Fields Including Effects of Compressibility," NASA TP-1517 (1980).
4. Wilcox, D.C. and Traci, R.M., "A Complete Model of Turbulence," AIAA Paper 76-351 (1976).
5. Cebeci, T., Kaups, K. and Ramsey, J.A., "A General Method for Calculating Three-Dimensional Compressible Laminar and Turbulent Boundary Layers on Arbitrary Wings," NASA CR-2777 (1977).
6. Keller, H.B., "A New Difference Scheme for Parabolic Problems," Numerical Solutions of Partial Differential Equations, II, J. Bramble (ed), Academic Press, New York (1970).
7. Flugge-Lotz, I. and Blottner, F.G., "Computation of the Compressible Laminar Boundary-Layer Flow Including Displacement-Thickness Interaction Using Finite-Difference Methods," AFOSR 2206, U.S. Air Force (Jan 1962).
8. Blottner, F.G., "Variable Grid Scheme Applied to Turbulent Boundary layers," Comp Meth Appl Mech & Eng, Vol 4, No 2, pp 179-194 (Sep 1974).
9. Wilcox, D.C. and James, R.M., "A Family of Explicit, Conservative, Unconditionally Stable Finite Difference Schemes," No Report Number, Douglas Aircraft Co, Long Beach CA (1969).
10. Krause, E., Comment on "Solution of a Three-Dimensional Boundary-Layer Flow With Separation," AIAA J, Vol 6, No 12, pp 575-576 (Mar 1969).
11. Larsson, L., "SSPA-ITTC Workshop on Ship Boundary Layers," (1980).
12. Hess, J.L. and Smith, A.M.O., "Calculation of Potential Flow About Arbitrary Bodies," Prog Aero Sci, Vol 8, Pergamon Press, Oxford and New York (1966).
13. Rao, G.N.V., "The Law of the Wall in a Thick Axisymmetric Boundary Layer," J of Basic Eng, Trans ASME, Ser D, Vol 89, p 237 (1969).
14. Richmond, R.L., "Experimental Investigation of Thick Axially Symmetric Boundary Layers on Cylinders at Subsonic and Hypersonic Speeds," PhD Thesis, California Inst of Tech (1957).

REFERENCES (Cont)

15. Patel, V.C., "A Unified View of the Law of the Wall Using Mixing-Length Theory," Aero Quarterly, Vol XXIV, pp 55-70 (Feb 1973).
16. Yu, Y.S., "Effect of Transverse Curvature on Turbulent Boundary Layer Characteristics," J of Ship Research, Vol 3, pp 33-51 (1958).
17. Patel, V.C., "A Simple Integral Method for the Calculation of Thick Axisymmetric Boundary Layers," IIHR Report No 150, Univ of Iowa (Sep 1973).
18. Patel, V.C., Nakayama, A. and Damian, R., "An Experimental Study of the Thick Turbulent Boundary Layer Near the Tail of a Body of Revolution," IIHR Report No 142, Univ of Iowa (Jan 1973).
19. Patel, V.C. and Lee, Y.T., "Thick Axisymmetric Turbulent Boundary Layer and Near Wake of a Low-Drag Body of Revolution," IIHR Report No 210, Univ of Iowa (Dec 1977).
20. Wilcox, D.C. and Chambers, T.L., "Streamline Curvature Effects on Turbulent Boundary Layers," AIAA Journal, Vol 15, No 4, pp 574-580 (Apr 1977).
21. Patel, V.C., "On the Equations of a Thick Axisymmetric Turbulent Boundary Layer," Iowa Inst of Hydraulic Research, IIHR Report No 143 (1973).
22. Wilcox, D.C., "User's Manual for PROGRAM SMOOTH: A Least-Squares Cubic-Spline Fit Routine," DCW Industries Report DCW-R-16-02 (1976).

APPENDIX: PROGRAM LISTINGS

This appendix has been omitted in the interest of economy. It contains complete program listings and input/output descriptions for the three programs SHPMSH, VELOC and EDDY3. To obtain a copy of this report including the Appendix, contact either the David W. Taylor Naval Ship Research and Development Center or DCW Industries, Inc.

UNCLASSIFIED

SECURITY CLASSIFICATION OF THIS PAGE (When Data Entered)

REPORT DOCUMENTATION PAGE		READ INSTRUCTIONS BEFORE COMPLETING FORM
1. REPORT NUMBER	2. GOVT ACCESSION NO.	3. RECIPIENT'S CATALOG NUMBER
4. TITLE (and Subtitle) BOUNDARY-LAYER DEVELOPMENT ON SHIP HULLS		5. TYPE OF REPORT & PERIOD COVERED FINAL REPORT 1 FEB 1981 - 31 JAN 1983
		6. PERFORMING ORG. REPORT NUMBER DCW-R-26-01 ✓
7. AUTHOR(s) DAVID C. WILCOX		8. CONTRACT OR GRANT NUMBER(s) N00014-81-C-0235
9. PERFORMING ORGANIZATION NAME AND ADDRESS DCW INDUSTRIES, INC. 4367 Troost Avenue Studio City, CA 91604		10. PROGRAM ELEMENT, PROJECT, TASK AREA & WORK UNIT NUMBERS
11. CONTROLLING OFFICE NAME AND ADDRESS DTNSRDC Bethesda, MD		12. REPORT DATE JANUARY 1983
		13. NUMBER OF PAGES 121
14. MONITORING AGENCY NAME & ADDRESS (if different from Controlling Office)		15. SECURITY CLASS. (of this report) UNCLASSIFIED
		15a. DECLASSIFICATION/DOWNGRADING SCHEDULE
16. DISTRIBUTION STATEMENT (of this Report) Approved for Public Release, Distribution Unlimited.		
17. DISTRIBUTION STATEMENT (of the abstract entered in Block 20, if different from Report)		
18. SUPPLEMENTARY NOTES		
19. KEY WORDS (Continue on reverse side if necessary and identify by block number) SHIP HYDRODYNAMICS, THREE-DIMENSIONAL BOUNDARY LAYERS, THICK BOUNDARY LAYERS		
20. ABSTRACT (Continue on reverse side if necessary and identify by block number) A three-dimensional boundary-layer computer program is developed which is suitable for application to arbitrary ship hulls. The program embodies the Wilcox-Rubesin two-equation model of turbulence. The numerical algorithm, based on the Blottner variable-grid method and the Krause explicit marching technique, is tested for two ship hulls and found to be accurate and stable for relatively large reverse crossflow. The program admits		

UNCLASSIFIED

SECURITY CLASSIFICATION OF THIS PAGE (When Data Entered)

rapid stretching of the grid normal to the surface and solutions become grid independent for mesh-point number in excess of about 60.

Comparisons between computed and measured momentum thickness for the two ship-hull computations indicate that, on the one hand, the Wilcox-Rubesin model improves predictive accuracy over that found at the 1980 SSPA-ITTC Workshop on Ship Boundary Layers. On the other hand, discrepancies between computation and measurement remains large enough to warrant further research. Because the computations use conventional thin-shear-layer approximations and discrepancies are largest near the stern, it appears likely that improved accuracy can only be obtained by accounting for the fact that the boundary layer becomes "thick".

To test the model for thick boundary layers, three submerged axisymmetric bodies are analyzed, viz, a thin cylinder aligned axially with the freestream and two bodies with adverse pressure gradient. Comparisons between computed and measured flow properties for the thin cylinder show the model to be quite accurate in the absence of pressure gradient. Using first the measured surface pressure distribution and then the measured boundary-layer-edge pressure distribution, experimental data are found to lie between the two computational results for both bodies. This result indicates that by accounting for the normal pressure gradient, model predictions for thick boundary layers should be very close to measurements. An integral method is devised and tested for computing the normal pressure gradient. Differences between computed and measured pressure distributions are well within experimental data scatter.